buildings

MDPI

Article

Fatigue Assessment of Weathering Steel Welded Joints Based on Fracture Mechanics and Machine Learning

Jianxing Du, Han Su * and Jinsheng Du

School of Civil Engineering, Beijing Jiaotong University, Beijing 100044, China
* Correspondence: hansu@bjtu.edu.cn

Abstract

To improve the computational efficiency of complex fatigue assessments, this study proposes a framework that integrates high-fidelity finite element analysis (FEA)with ensemble learning for evaluating the fatigue performance of weathering steel welded joints. First, a three-dimensional crack propagation model for cruciform fillet welds was developed on the ABAQUS-FRANC3D platform, with a validation error of less than 20%. Subsequently, a large-scale parametric analysis was conducted. The results indicate that as the stress amplitude increases from 67.5 MPa to 99 MPa, the fatigue life decreases to 40.29% of the baseline value. When the stress amplitude reaches 180 MPa, the fatigue life drops sharply to 14.28% of the baseline. Within the stress ratio range of 0.1 to 0.7, increasing the initial crack size from 0.075 mm to 0.5 mm reduces the fatigue life to between 85.78% and 86.48% of the baseline. Edge cracks, influenced by stress concentration, exhibit approximately 15.2% shorter fatigue life compared to central cracks, while the maximum variation in fatigue life due to crack geometry is only 10.25%. Second, an Extremely Randomized Trees surrogate model constructed based on the simulation data demonstrates excellent performance. Finally, by integrating this model with Paris's law, the developed prediction framework achieves high consistency with numerical simulation results, with all predicted values falling within the two-standard-deviation interval. This data-driven approach can effectively replace computationally intensive finite element analysis, enabling efficient structural safety assessments.

Keywords: weathering steel; fatigue life prediction; fracture mechanics; crack propagation; ensemble learning; surrogate model

1. Introduction

Welded structures are widely employed in bridge construction owing to their high strength and versatility. Weathering steel, recognized for its superior corrosion resistance and durability, is commonly used in such applications. However, the quality of welded joints plays a critical role in determining the fatigue performance of these structures. During welding, defects such as initial cracks and weld misalignment may occur, compromising the structural fatigue life. These defects act as stress concentrators, accelerating the propagation of fatigue cracks. The fatigue life of welded joints is influenced by various factors, including the initial crack size, crack location, and crack geometry, all of which must be carefully considered in the design and maintenance of welded weathering steel structures.

The influence of initial crack size, location, and geometry on fatigue life has been investigated in a number of studies employing conventional experimental and numerical approaches. Su et al. and Lawrence, for instance, examined how initial crack dimensions

Check for updates

Academic Editor: Salvatore Verre

Received: 23 December 2025
Revised: 15 January 2026
Accepted: 16 January 2026
Published: 18 January 2026

Copyright: © 2026 by the authors. Licensee MDPI, Basel, Switzerland. This article is an open access article distributed under the terms and conditions of the Creative Commons Attribution (CC BY) license.

and positioning affect the fatigue performance of welded steel joints [1,2]. Their findings indicate that cracks located at the weld toe or within the base material markedly reduce fatigue life by promoting accelerated crack propagation. Furthermore, research conducted by Azar et al. and Hu et al. elucidated the contribution of weld misalignment to fatigue crack initiation in the heat-affected zone (HAZ) [3,4]. From a fracture mechanics standpoint, Hang [5] applied the Extended Finite Element Method (XFEM) to compute stress intensity factors in ship cruciform joints, underscoring the utility of numerical methods in capturing complex crack behavior. Additionally, the versatility of finite element analysis (FEA) validated by experimental data has been demonstrated in various structural applications, such as the seismic strengthening assessment of reinforced concrete columns [6], confirming the reliability of numerical approaches in predicting complex structural responses. In a similar vein, Takanashi et al. [7] underscored the significance of crack initiation in large-scale specimens and stressed the necessity of accurately modeling initial defects for reliable fatigue life predictions.

Despite these advances, traditional finite element analysis (FEA) and fracture mechanics approaches continue to face challenges in computational efficiency, particularly when handling complex loading conditions and extensive parametric studies [8]. To address these limitations, data-driven approaches and machine learning (ML) have recently emerged as powerful tools for fatigue assessment [9–13]. Zhang et al. [14] proposed an ML-based framework for predicting the fatigue life of three-dimensional cracked specimens, successfully modeling the complex relationship between geometric parameters and fatigue life. This data-driven trend has been further extended to tubular T-joints by Zhang et al. [15], who combined fracture mechanics with ML to predict crack propagation under multiaxial loading. Moreover, Kamble et al. [16] and Sun and Huang [17] demonstrated that ML algorithms can accurately predict fatigue crack growth rates and propagation life, providing a rapid alternative to computationally intensive simulations.

The application of machine learning in fatigue prediction has been validated across multiple engineering domains. For example, Al-Hagri et al. [18] employed multi-fidelity modeling to predict fatigue crack propagation in offshore steel jacket structures, balancing computational cost with accuracy. In the field of advanced manufacturing, Huang [19] applied machine learning to predict the fatigue life of additively manufactured lightweight alloys. Specific algorithms have also demonstrated potential: Xie [20] utilized a BO-MLP neural network to analyze turbocharger pipelines, while Chen [21] applied deep belief networks to assess the reliability of cable-stayed bridge structures. These studies indicate that integrating physics-based simulations with machine learning surrogate models enables efficient and accurate structural assessment. Furthermore, Wang et al. [22] developed an artificial neural network-based approach to predict the fatigue life of threaded connections and estimate critical distances. Wang et al. [23] investigated the predictive performance of different backpropagation neural network architectures for three-dimensional elliptical crack propagation. Ma et al. [24] proposed a network architecture that takes crack length increment information as input and outputs the corresponding cycle count, improving prediction accuracy in data-limited scenarios. Additionally, Kotousov et al. [25] adopted a data-driven method to evaluate crack-tip opening loads in aerospace-grade aluminum alloy CT specimens under variable amplitude loading, with results showing good agreement with experimental and numerical simulations. Wang et al. [26] established a mapping relationship between deflected crack geometry and crack-tip stress intensity factors using Gaussian process surrogate models.

Building upon recent advances in fatigue assessment methodologies [27–30], this study proposes a hybrid framework that synergizes the high fidelity of numerical simulations with the computational efficiency of machine learning. By leveraging the advantages of

both approaches, it aims to bridge the gap between complex fracture mechanics analysis and rapid engineering prediction. Specifically, this work investigates the effects of stress amplitude, initial crack size, crack location, and crack geometry on the fatigue life of welded weathering steel joints. Through integrated numerical simulations and experimental validation, this work systematically examines how these factors influence fatigue life and crack propagation behavior in such joints. Furthermore, building upon the simulation dataset, this research develops a robust machine learning model for predicting key fracture mechanics parameters. The significance of this study lies in providing theoretical foundations and methodological support for the design and maintenance of welded weathering steel structures, particularly in bridge engineering. By elucidating the combined influence of stress amplitude, initial crack size, location, and crack geometry, and by employing data-driven predictive tools, the findings offer scientific insights for optimizing welding techniques and material selection. This contributes to more accurate fatigue life prediction models, ultimately enhancing the safety, reliability, and durability of welded steel bridge structures. The main research content of this paper is illustrated in Figure 1.

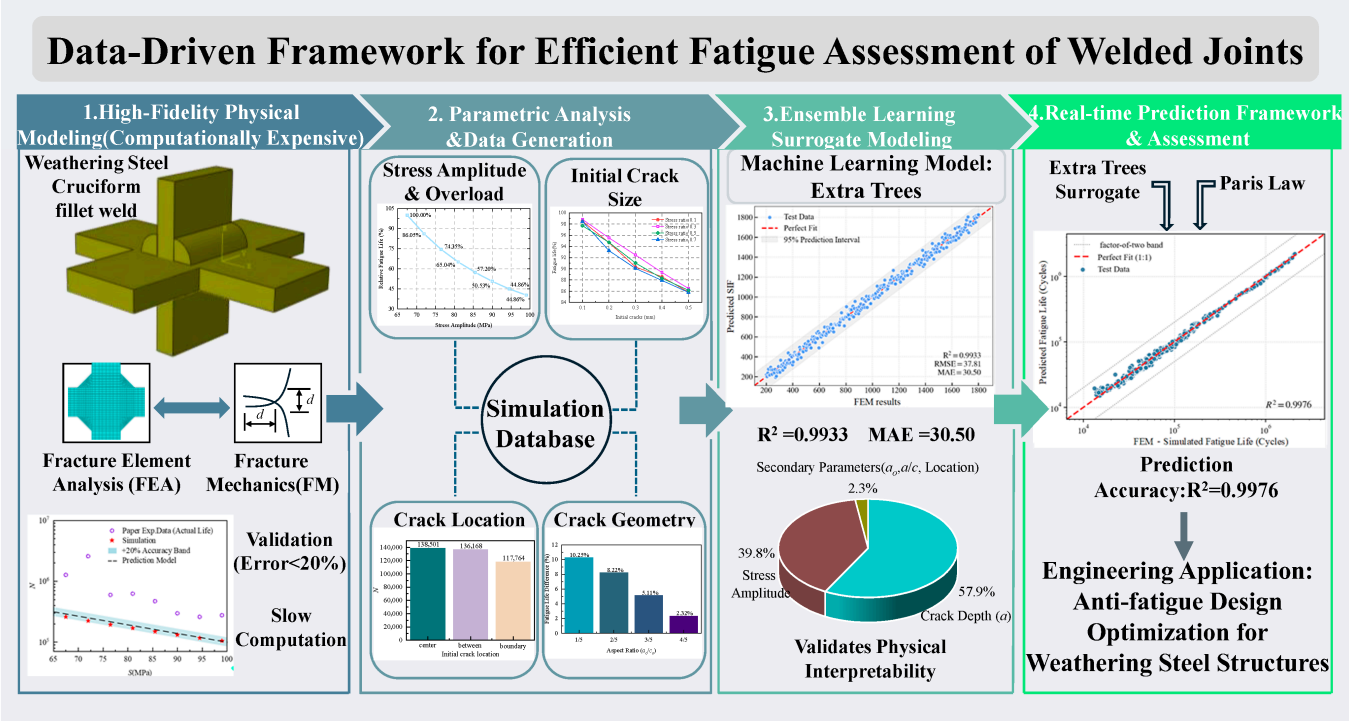


Figure 1. A framework for anti-fatigue design optimization of weathering steel welded joints based on hybrid numerical simulation and ML aid. The diagram illustrates the research workflow, where arrows indicate the logical data flow between modules. The inset graphs display representative parametric trends, with the blue line specifically depicting the non-linear degradation of fatigue life under varying load conditions.

2. Numerical Simulation Methodology

2.1. Fatigue Life Assessment Methodology for Weathering Steel

This study develops a numerical simulation methodology and a life assessment system for fatigue crack propagation in weathering steel, grounded in the finite element method and the theoretical framework of linear elastic fracture mechanics [31]. Leveraging the ABAQUS-FRANC3D co-simulation platform, a multiphysics coupling approach is employed to achieve high-fidelity numerical simulation of the entire process from initial crack initialization to fatigue-driven propagation. Specifically, a baseline finite ele-

ment model is first established in ABAQUS 2020 (Dassault Systèmes, Vélizy-Villacoublay, France),incorporating comprehensive material constitutive relations, a refined mesh topology, and precisely defined boundary conditions (bottom-fixed and cyclic loading applied at the top). This model is subsequently transferred to the FRANC3D 8.5 (Fracture Analysis Consultants, Inc., Ithaca, NY, USA) environment, where initial cracks are introduced in regions of stress concentration based on the maximum principal stress criterion. A hybrid element discretization strategy is adopted: the crack-tip singular zone is locally refined using 20-node wedge and hexahedral elements with a graded element size transition ranging from 1 to 4 mm [32], while the remaining domains are discretized with 10-node tetrahedral elements [33]. Through iterative FRANC3D-ABAQUS coupled solving, the displacement field is computed, the crack front is updated, and adaptive remeshing is performed until the crack reaches a critical dimension, at which point the simulation terminates. The complete workflow is schematically illustrated in Figure 2.

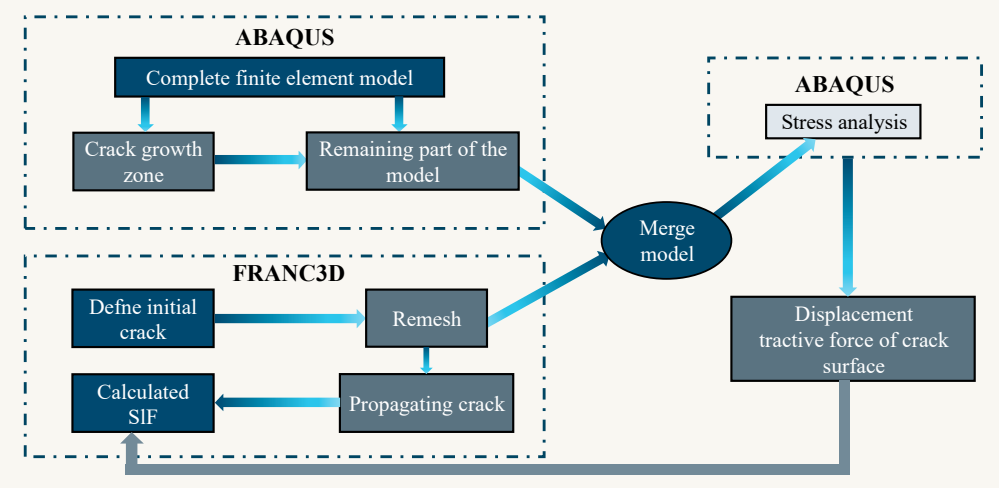


Figure 2. Integrated simulation workflow of ABAQUS-FRANC3D coupling analysis.

In the FRANC3D computational framework, three methodologies are available for calculating stress intensity factors (SIFs): the M-integral (interaction integral) method, the displacement correlation method, and the virtual crack closure technique (VCCT). Among these, the M-integral method was employed in this study due to its superior numerical accuracy in resolving crack-tip stress fields [28]. For determining crack propagation trajectory, the software provides five criteria: maximum tangential stress (MTS), maximum shear stress, generalized stress, strain energy release rate, and planar extension. The maximum tangential stress (MTS) criterion was adopted here, as its validity has been widely verified experimentally [34].

To quantify the effective stress intensity factor range (ΔK_{eff}), both the Mode-I (Opening Mode) formulation and the Mixed-Mode (superposition of Opening, Sliding, and Tearing modes) formulation are applicable [33]. The simulation follows a quasi-static crack growth process. While the crack propagation path is adaptively updated based on the MTS criterion, a fixed (predetermined) crack extension increment (Δa) is applied for each calculation step. Fatigue life is then computed iteratively based on Equation (1).

$$N = \sum_{1}^{n} N_i = \sum_{1}^{n} \int_{a_0}^{a_{cr}} \frac{da}{C(\Delta K)^m} = \int_{a_0}^{a_{cr}} \frac{da}{C(\Delta K)^m} \quad (1)$$

where N is the number of fatigue cycles; a_0 is the initial crack size; a_i is the predetermined crack propagation step length; a_{cr} is the critical crack size; and C and m are fatigue crack growth rate parameters.

2.2. Finite Element Model

Based on the standardized specimen geometry specified in Ref. [33], this study established a three-dimensional finite element model with strict dimensional consistency. The key geometric features of the referenced specimen are illustrated in Figure 3, which served as the basis for the FE model construction. All dimensional parameters were directly adopted from the experimentally validated data provided in Ref. [33], ensuring full geometric similarity between the numerical model and the physical specimens. The model topology was rigorously verified, with all geometric features maintaining the same relative positional relationships and dimensional proportions as those of the reference specimen, thereby establishing a precise geometric basis for subsequent fracture mechanics analysis. The modeling approach guarantees the following: (1) exact replication of weld toe radii (ρ = 0.5 mm) and flank angles (θ = 45°), (2) precise positioning of initial crack insertion sites, and (3) correct representation of thickness transitions in cruciform joint regions.

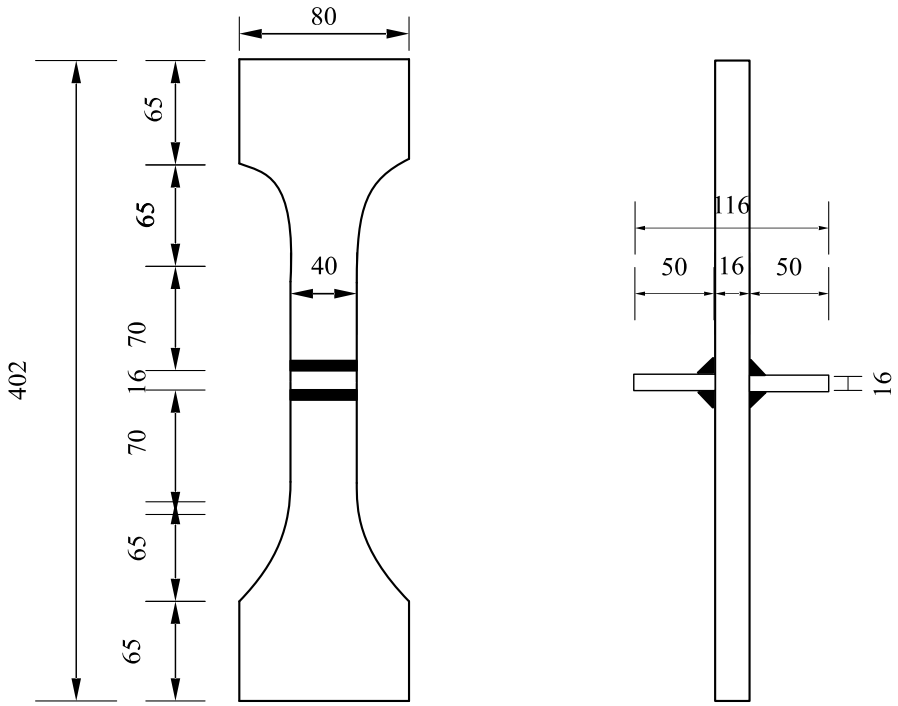


Figure 3. Geometric configuration of fatigue-critical detail (unit: mm).

Based on experimental characterization data from Ref. [33], this study developed ABAQUS finite element models using representative geometric parameters. Instead of adopting measurements from individual specimens, statistically averaged values of key morphological features—including misalignment (e), plate thickness (t), and weld leg lengths (h and v)—were used as model inputs (Table 1). As shown in Figure 4, these normalized parameters comprehensively capture the specimen's morphological characteristics, encompassing weld toe geometry and thickness transitions. By implementing these statistically derived dimensions, fabrication-induced stochastic heterogeneity was effectively mitigated, thereby enabling a representative evaluation of structural performance. Anchored in empirical data from Ref. [33], this modeling approach preserves the critical stress concentration features essential for accurate fracture mechanics analysis.

Table 1. Mean values of geometric measurements for cruciform fillet welds.

	e (mm)	t (mm)	Fillet Weld 1		Fillet Weld 2		Fillet Weld 3		Fillet Weld 4	
			h_1 (mm)	v_1 (mm)	h_2 (mm)	v_2 (mm)	h_3 (mm)	v_3 (mm)	h_4 (mm)	v_4 (mm)
Arithmetic Mean	1.07	16.25	8.20	8.12	8.22	8.26	8.46	8.25	8.51	8.27

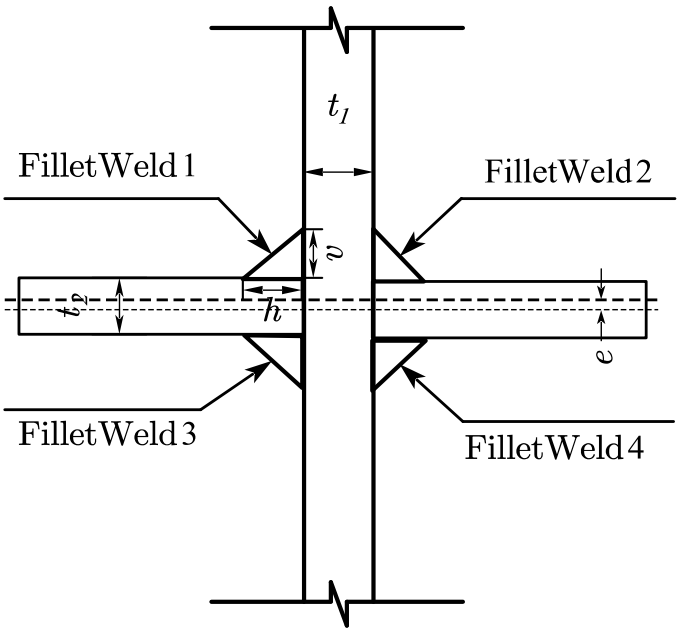


Figure 4. Geometric characterization of test specimen. The arrows indicate geometric dimensions and component labels, while the dashed lines represent the centerlines of the plates, highlighting the misalignment (eccentricity) denoted by e.

Based on the standardized geometric parameters provided in Table 1, a three-dimensional finite element model of a cruciform fillet-welded joint was developed in ABAQUS. The model was discretized using 20-node quadratic brick elements (C3D20) with full integration, following a graded mesh refinement approach. As shown in Figure 5a, the element size transitioned from 1 mm in critical zones (weld toe and heat-affected zones) to 4 mm in far-field regions. Static analysis results (Figure 5b) reveal significant stress concentration at the weld toe, with the peak stress reaching 410 MPa (Figure 5c). The boundary conditions were explicitly defined with reference to the global coordinate system shown in Figure 5a: the nodes at the base surface were fully constrained in all translational degrees of freedom ($U_x = U_y = U_z = 0$). On the top surface, a constant uniform tensile load equivalent to the peak stress ($\sigma_{\max}$) was applied to simulate the maximum loading condition of the fatigue cycle. An isotropic linear elastic constitutive model is adopted, with material properties (E = 206 GPa, ν = 0.3) directly referenced from [33]. The yield strength of the welded weathering steel is 426 MPa, which exceeds the calculated peak stress of 410 MPa. Furthermore, the plastic zone size formed at the crack tip satisfies the small-scale yielding condition relative to the crack length, thereby justifying the applicability of linear elastic fracture mechanics and validating the assumption of predominantly elastic deformation throughout the loading history. This establishes a rigorous foundation for the subsequent fatigue crack propagation analysis.

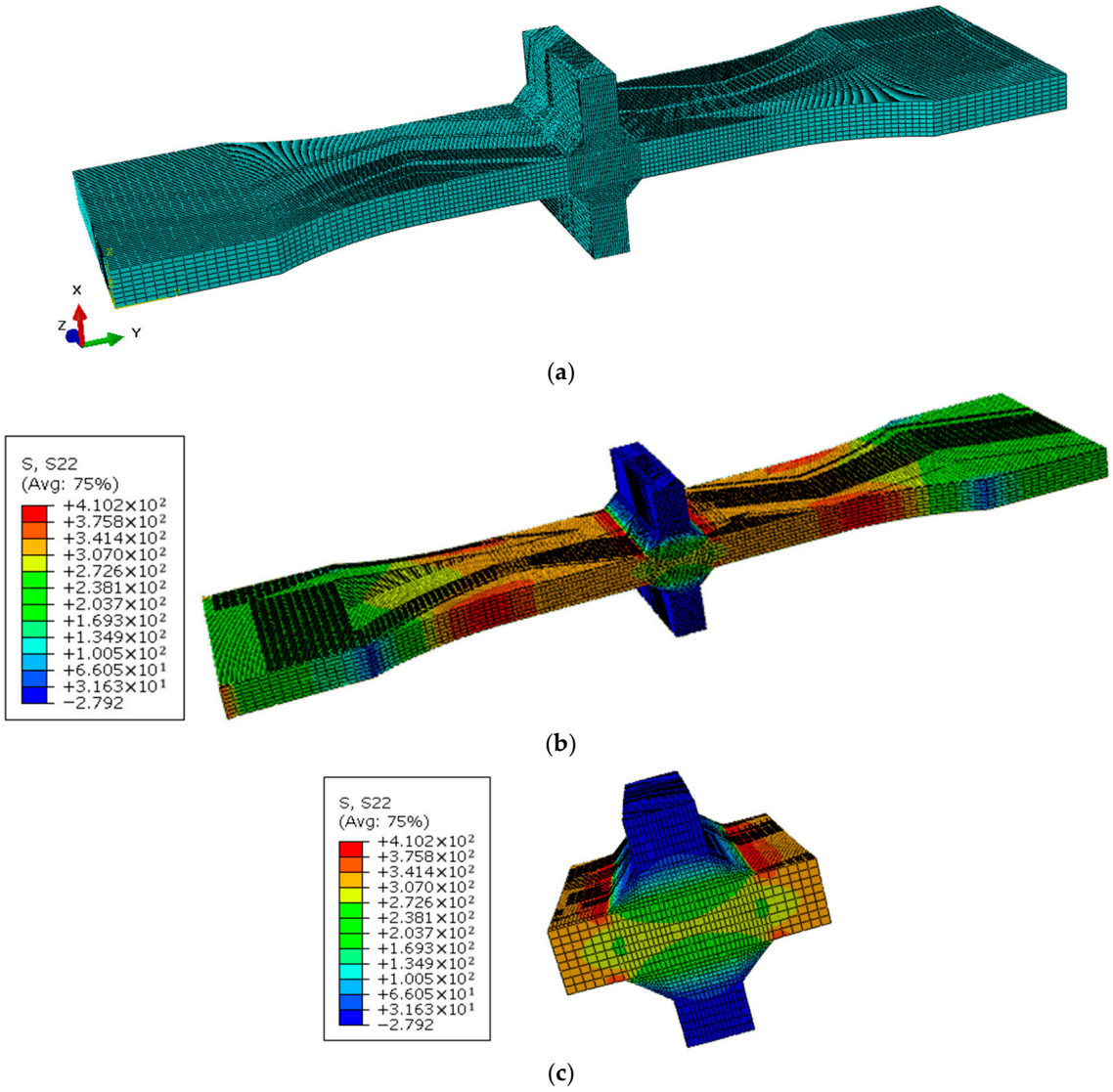


Figure 5. Finite element modeling and analysis results in ABAQUS. (**a**) Finite element discretization model, (**b**) static stress distribution contour plot, and (**c**) cruciform fillet weld stress analysis contour.

2.3. Evaluation Procedure

Stress analysis in Figure 5c reveals a symmetric stress distribution, with identical peak stress values of 410 MPa occurring at both the upper and lower weld toes. Due to the equivalent stress concentration severity in these critical regions, the lower weld toe was selected as the representative location for initial crack insertion. The critical crack size (a_{cr}) was defined to be equal to the plate thickness (16 mm). Following the methodology established in Ref. [33], the fatigue crack propagation kinetics were characterized using Paris law parameters $\log C = -10.37$ and $m = 2.38$ (where da/dN is expressed in mm/cycle and ΔK in MPa·mm$^{1/2}$). It is worth noting that the exponent $m = 2.38$, derived experimentally for this weathering steel [33], differs distinctively from the typical value of $m \approx 3.0$ commonly used for ordinary structural steels (e.g., in BS7910 standards [35]). This lower m value reflects the specific crack propagation resistance of the weathering steel material used in this study, justifying the necessity of using material-specific parameters rather than generic steel data for accurate life assessment. A zero-threshold assumption ($\Delta K_{eff} = 0$) was applied, effectively extending the Paris law into the near-threshold regime (Region I), thereby producing conservative fatigue life predictions consistent with the experimental validation reported in the referenced study.

Guided by the stress contour distribution obtained from the ABAQUS static analysis, the global finite element model was imported into the FRANC3D fracture mechanics platform. Numerical results identified a significant stress concentration in the central region of the lower weld toe, which was consequently designated as the initial crack insertion site. To accurately resolve the crack-tip singularity, an advanced adaptive mesh refinement strategy was implemented, as visualized in Figure 6. The discretization scheme employs a hybrid topology: (i) 15-node wedge elements (singular elements) and 20-node hexahedral elements are deployed in the immediate vicinity of the crack front ($r \leq 0.5$ mm) to capture the high-stress gradients; and (ii) 10-node tetrahedral elements are utilized to mesh the far-field regions, ensuring a smooth transition.

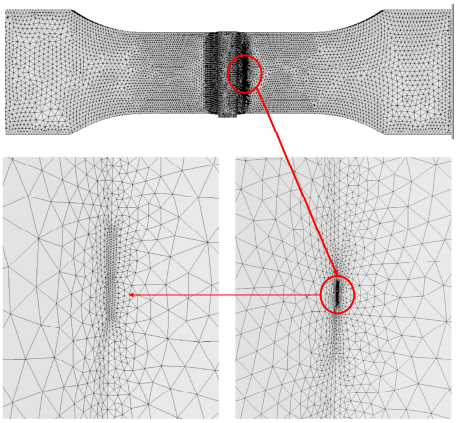


Figure 6. Computational implementation of initial crack insertion and adaptive mesh refinement. The red circles and arrows illustrate the detailed view process, indicating the transition from the global mesh to the local refined mesh around the crack tip.

The fracture mechanics parameters were evaluated based on a standard local crack-tip polar coordinate system:

(1) Stress intensity factors (SIFs): The path-independent M-integral method was employed to accurately calculate the Mixed-Mode SIFs (K_I, K_{II}, K_{III}) utilizing the integration domain defined by the local coordinates (r, θ, z) originating at the crack front.

(2) Propagation trajectory: Based on the calculated SIFs, the maximum tangential stress (MTS) criterion was adopted to determine the crack propagation direction. Specifically, the crack is assumed to propagate along the angle where the tangential stress component ($\sigma_{\theta\theta}$) is maximized.

(3) Driving force: Quantified using an equivalent stress intensity factor range (ΔK_{eff}) model to account for Mixed-Mode (I, II, III) coupling effects [34].

$$\Delta K_{eff} = \sqrt{K_I^2 + {K_{II}}^2 + \frac{K_{III}^2}{(1-v)}} \quad (2)$$

where K_I is the stress intensity factor amplitude caused by normal stress, K_{II} is the stress intensity factor amplitude caused by shear stress, K_{III} is the stress intensity factor amplitude caused by torsional stress, and v is Poisson's ratio, with a value of 0.3 [33].

2.4. Evaluation Results and Analytical Findings

Based on the driving force determined by Equation (2), the fatigue crack propagation process was simulated by incorporating the Paris law. Using the standardized specimen geometry and calibrated material parameters, this study systematically investigated the fatigue behavior under constant-amplitude cyclic loading with a stress ratio of R = 0.1. An initial semicircular surface crack (a_0 = 0.28 mm) was introduced at the location of maximum

stress (the center of the lower weld toe). Crack propagation was then simulated iteratively over a range of stress amplitudes ($\Delta\sigma$ = 67.5–99 MPa) until the critical depth was reached. By compiling the total fatigue life cycles computed for each stress level, a material-specific stress–life (*S*-*N*) curve was constructed, as shown in Figure 7. This curve quantitatively characterizes the fatigue resistance of the welded weathering steel joint and provides a benchmark for subsequent life assessment.

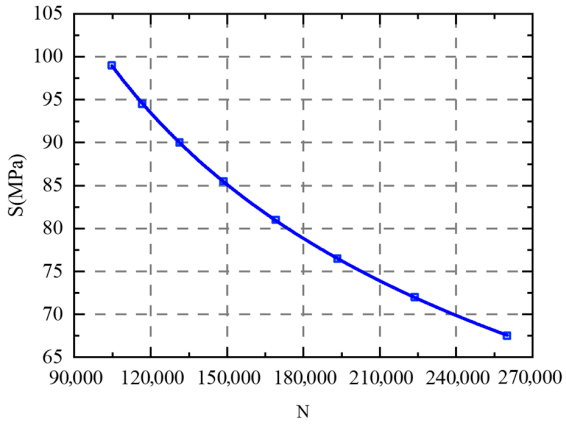


Figure 7. Stress–life (*S*-*N*) characterization of fatigue performance. The blue line represents the fitted *S*-*N* curve connecting the data points, illustrating the decreasing trend of fatigue life with increasing stress amplitude.

Figure 8 presents a comparative validation between the numerical simulation results obtained from FRANC3D and the experimental data reported in the literature, along with the corresponding prediction model. The results indicate that the predictions from the numerical model developed in this study (red stars) show a high degree of agreement with the baseline prediction model provided in the literature (paper prediction model, black dashed line) throughout the entire fatigue life. Specifically, all simulation data points fall precisely within the 20% accuracy band of the prediction model, and their variation trend closely aligns with the theoretical curve, confirming the robustness of the numerical method in simulating crack propagation and predicting fatigue life. Moreover, compared with the experimental data (blue circles), which exhibit considerable scatter, the numerical simulation results consistently adhere to the "conservative baseline." This demonstrates that the model effectively mitigates the influence of random experimental errors and provides lower-bound predictions with adequate safety margins, which is consistent with the conservative principles inherent in engineering structural fatigue design.

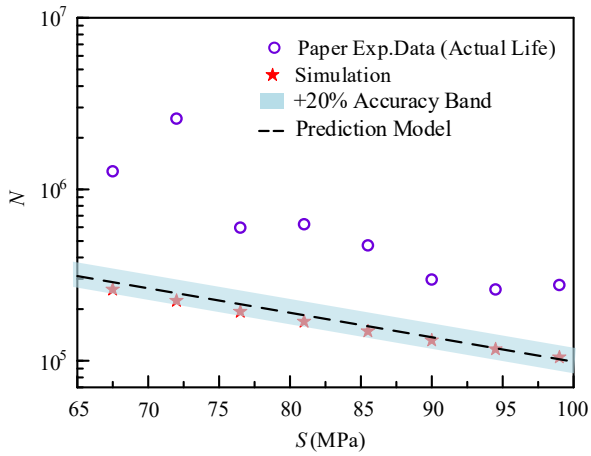


Figure 8. Model validation through experimental–numerical correlation analysis [33].

3. Parametric Analysis of Fatigue Life Influencing Factors

The numerical analysis evaluates crack growth behavior and fatigue life through systematic computation of the crack-tip stress intensity factor (SIF), particularly in propagation simulations. It should be noted that although initial verification of model validity considered crack propagation through the full plate thickness (16 mm), a more appropriate failure criterion is required for the parametric analysis in this section. For load-bearing plate structures, rapid fracture occurs once the surface crack depth reaches half of the plate thickness (a/t = 0.5, i.e., 8 mm). Therefore, distinguishing from the propagation criterion, this section adopts a geometric failure criterion where a critical crack depth of 8 mm (a/t = 0.5) defines the end of the safe fatigue life (critical usability limit).

3.1. Stress Amplitude Effects

Numerical simulations were performed on semicircular surface cracks (a_0 = 0.28 mm) initiated at the specimen center, spanning a range of stress amplitudes from 67.5 to 99 MPa. Figure 9 illustrates the distribution of the effective stress intensity factor (ΔK_{eff}) along the normalized crack front. The profiles reveal a characteristic heterogeneous distribution, where ΔK_{eff} exhibits peak values at the free surfaces (crack tips) and a local minimum at the deepest point (midpoint).

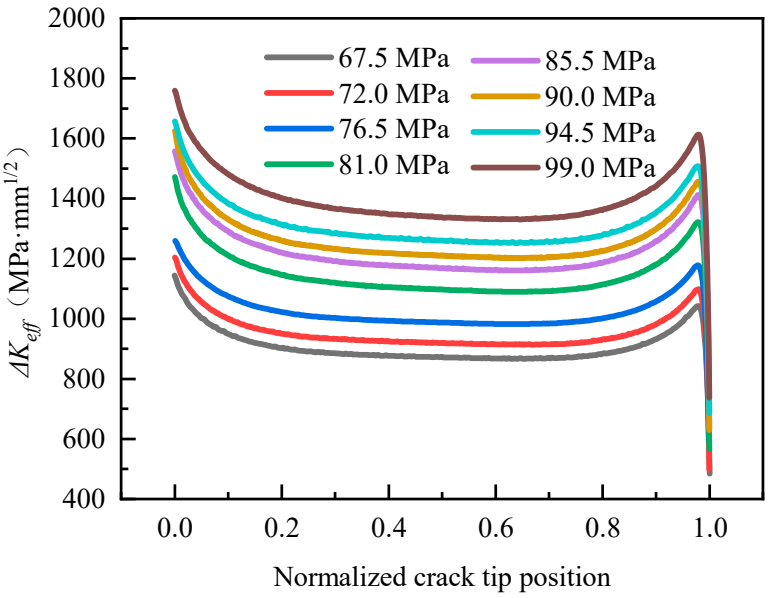


Figure 9. Crack-tip stress intensity factor evolution during propagation. Note: The normalized positions 0 and 1 correspond to the intersection points with the free surface, while the midpoint represents the deepest point of the crack front.

The macroscopic fatigue response is summarized in Figure 10, which presents both the crack propagation kinetics (a vs. N) and the resulting stress–life (S-N) curve. As detailed in Table 2, the maximum crack-tip driving force demonstrates a near-linear correlation with the applied stress amplitude.

Table 2. Maximum ΔK_{eff} values under different stress amplitudes (MPa).

The maximum crack-tip stress intensity factors MPa·mm$^{1/2}$	**Stress Amplitude (MPa)**							
	67.5	72	76.5	81	85.5	90	94.5	99
	1144	1204	1260	1471	1557	1625	1656	1760

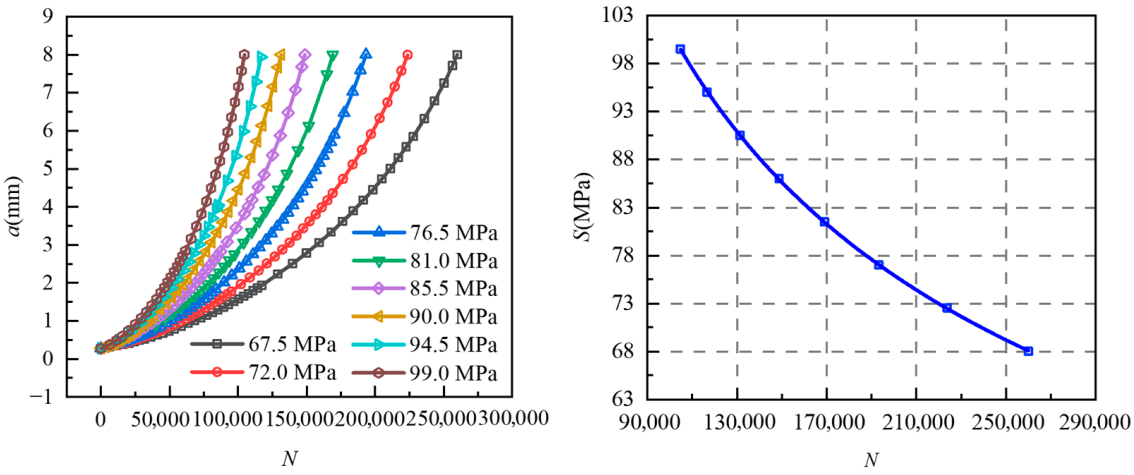


Figure 10. Stress–life (*S*-*N*) relationship for cruciform fillet welds. The blue line represents the fitted *S*-*N* curve connecting the data points, illustrating the decreasing trend of fatigue life with increasing stress amplitude.

Figure 11 further quantifies the sensitivity of fatigue life to load increments. Relative to the baseline condition (67.5 MPa), a distinct nonlinear decay in fatigue life is observed as stress amplitude increases. For instance, increasing the stress amplitude to 99 MPa reduces the fatigue life to approximately 40.29% of the baseline value. This trend reflects a characteristic acceleration in damage accumulation, following an inverse power-law relationship consistent with crack growth kinetics dominated by the Paris regime.

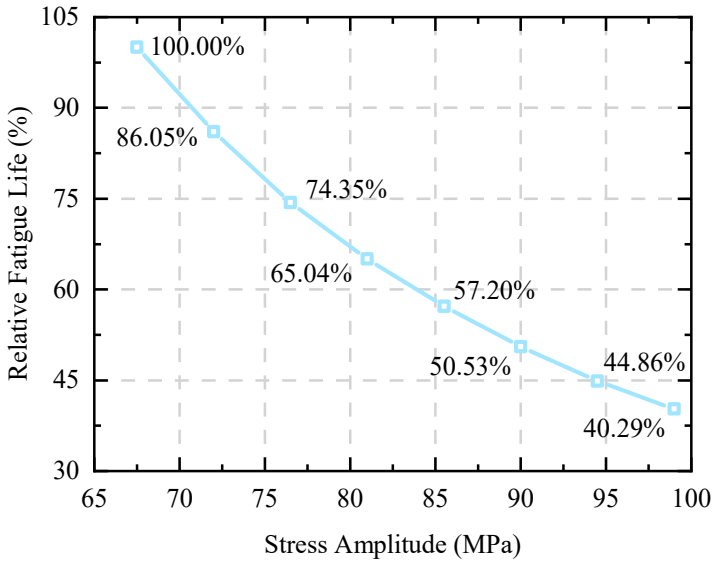


Figure 11. Effect of stress amplitude on fatigue life of cruciform fillet weld (a_0 = 0.28 mm). The blue line illustrates the non-linear degradation trend of relative fatigue life as stress amplitude increases.

The preliminary analysis was conducted based on an initial crack size of a_0 = 0.28 mm under standard service loads (67.5–99 MPa). However, considering the inevitable manufacturing defects in practical engineering and the resolution limits of Non-Destructive Testing (NDT), larger macroscopic cracks may exist. Furthermore, to comprehensively evaluate the structural safety under extreme overloading conditions, a subsequent analysis was performed considering a "worst-case scenario" with a larger initial defect (a_0 = 0.5 mm) and significantly higher stress amplitudes (up to 180 MPa).

To elucidate the fracture mechanics governing the potential failure under these extreme conditions, Figure 12 presents the evolution of the effective stress intensity factor range

(ΔK_{eff}) along the normalized crack front. The curves exhibit a characteristic "U-shape" profile, where the stress intensity is highest at the free surfaces (positions 0 and 1) compared to the deepest point of the crack (position 0.5), indicating that crack propagation is primarily driven by surface stress concentrations.

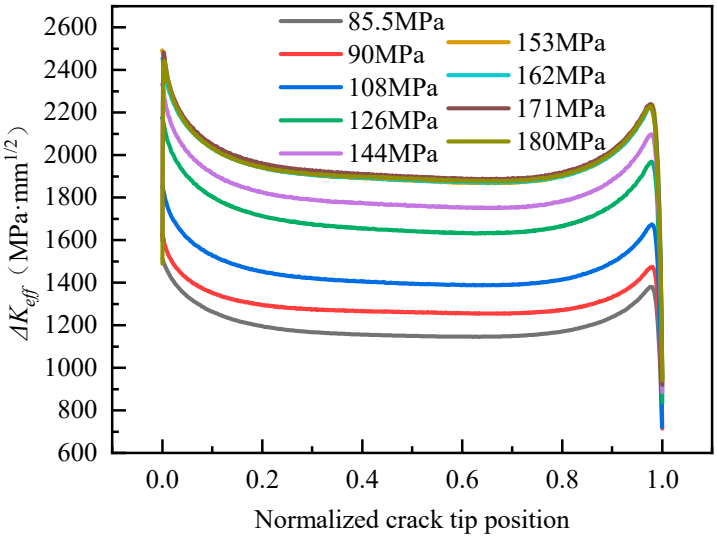


Figure 12. Crack-tip stress intensity factor evolution during propagation.

Quantitative data listed in Table 3 further reveal the severity of the high-stress conditions. As the stress amplitude increases from the baseline of 85.5 MPa to the extreme case of 180 MPa, the maximum crack-tip driving force surges from 1514 to 2444 MPa·mm$^{1/2}$. This substantial amplification in driving force directly correlates with the accelerated crack growth rates observed in the subsequent fatigue life analysis.

Table 3. Maximum ΔK_{eff} values under different stress amplitudes (MPa).

The maximum crack-tip stress intensity factors MPa·mm$^{1/2}$	**Stress Amplitude (MPa)**								
	85.5	90	108	126	144	153	162	171	180
	1514	1625	1853	2175	2333	2493	2455	2483	2444

The crack depth evolution kinetics, illustrated in Figure 13a, demonstrate a distinct stress-dependent transition in failure mechanisms. While the specimen subjected to a lower stress amplitude of 85.5 MPa exhibits a prolonged phase of stable propagation, the trajectory for the 180 MPa case becomes precipitously steep. This strongly nonlinear behavior is fundamentally governed by the power-law relationship inherent in Paris's law, where the fatigue life N is inversely proportional to the stress amplitude raised to the material exponent m (i.e., $N \propto (\Delta\sigma)^{-m}$). Given the specific material exponent m = 2.38 used in this study, the driving force for crack propagation increases exponentially with stress, causing the trajectory to transition to instantaneous instability almost immediately following crack initiation. Crucially, the comparative *S*-*N* analysis in Figure 13b highlights the sensitivity of fatigue life to initial defect dimensions. A discernible degradation in fatigue performance is observed between the baseline condition (a_0 = 0.28 mm, blue profile) and the enlarged defect scenario (a_0 = 0.50 mm, purple profile). This comparison quantitatively demonstrates that the presence of macroscopic defects significantly compromises the structural safety margin, particularly by accelerating the consumption of fatigue life in the high-cycle regime. However, it is worth noting that the reduction in fatigue life caused by defect enlargement is relatively moderate compared to the impact of stress amplitude. This

disparity is theoretically grounded in the integration of Paris's law. While fatigue life scales with stress amplitude as $(\Delta\sigma)^{-m}$ (exponent = 2.38), it scales with initial crack size as $a_0^{(1-m/2)}$ (exponent = 0.19). The order-of-magnitude difference in these sensitivity indices (2.38 vs. 0.19) explains why the structural life is mathematically far more sensitive to load variations than to initial geometric imperfections within the investigated range.

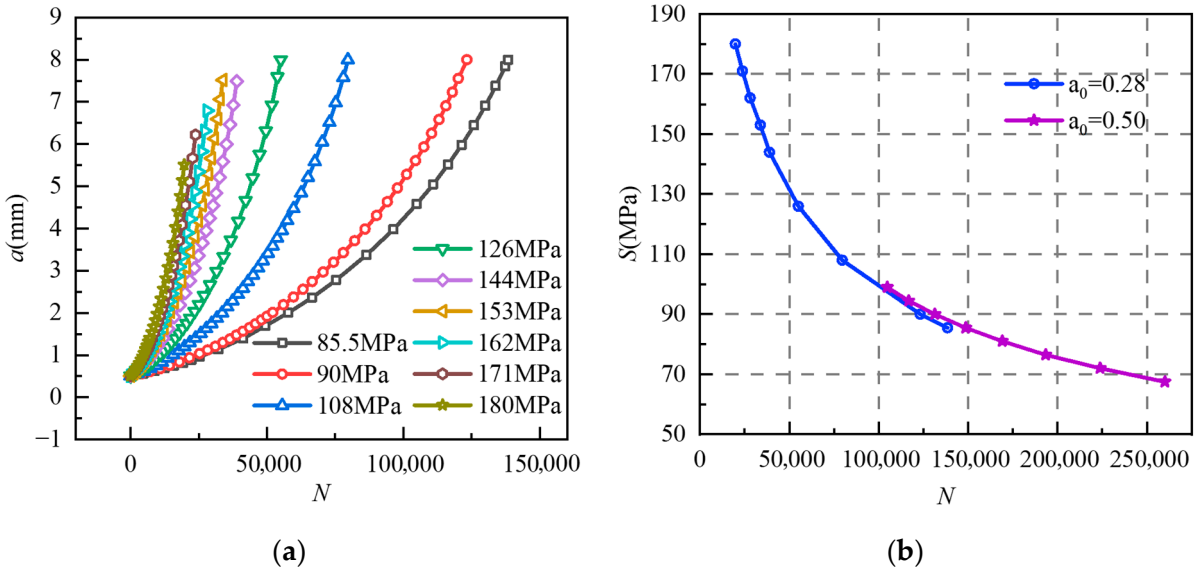


Figure 13. Fatigue crack propagation and S-N curves of cruciform fillet welds. (**a**) Fatigue crack propagation curve, (**b**) S-N for different initial defect dimensions.

To quantify this structural vulnerability, the relative degradation of fatigue life is analyzed in Figure 14. Normalization against the baseline condition (85.5 MPa) reveals a distinct nonlinear decay trend. Most notably, when the stress amplitude increases to 180 MPa, the fatigue life decreases sharply to only 14.28% of the baseline value. This pronounced reduction not only underscores the necessity for stringent defect control but also indicates a significantly elevated risk of rapid fracture under combined extreme overload and macroscopic cracking.

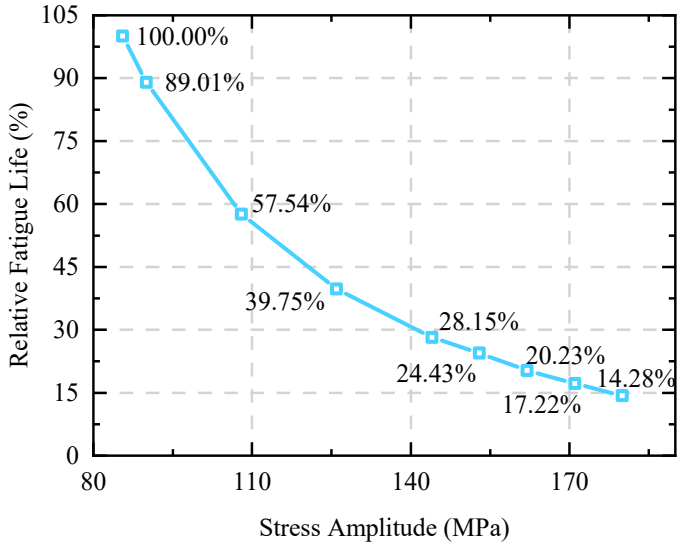


Figure 14. Relative fatigue life degradation profile under varying stress amplitudes (a_0 = 0.5 mm). The blue line illustrates the non-linear degradation trend of relative fatigue life as stress am-plitude increases.

3.2. Effects of Initial Crack Size

To elucidate the influence of initial crack dimensions on fatigue performance, numerical simulations were conducted to evaluate the evolution of the effective stress intensity factor range (ΔK_{eff}) in cruciform fillet-welded specimens containing semicircular cracks. Under constant-amplitude loading ($\Delta\sigma$ = 85.5 MPa), this study examined four stress ratios (R = 0.1–0.7) and six initial crack sizes (a_0 = 0.075–0.5 mm), as illustrated in Figure 15. The results show that ΔK_{eff} exhibits a characteristic "U-shaped" distribution along the crack front, with peak values occurring at the surface intersections and the lowest values at the deepest point. Notably, the midpoint ΔK_{eff} shows a positive correlation with the initial crack size, increasing progressively with larger a_0. Table 4 summarizes the maximum ΔK_{eff} values, confirming that larger initial defects lead to intensified crack-tip driving forces. Correspondingly, the fatigue life results presented in Figure 16 demonstrate a significant reduction in structural longevity with increasing initial flaw dimensions. It is observed that the dependence of fatigue life on the initial crack size generally follows a nonlinear inverse trend. However, this trend exhibits varying degrees of curvature under different stress ratios. For instance, the nonlinearity is most significant at R = 0.7, whereas at R = 0.3 and 0.5, the degradation of fatigue life approximates a linear behavior within the investigated range of a_0.

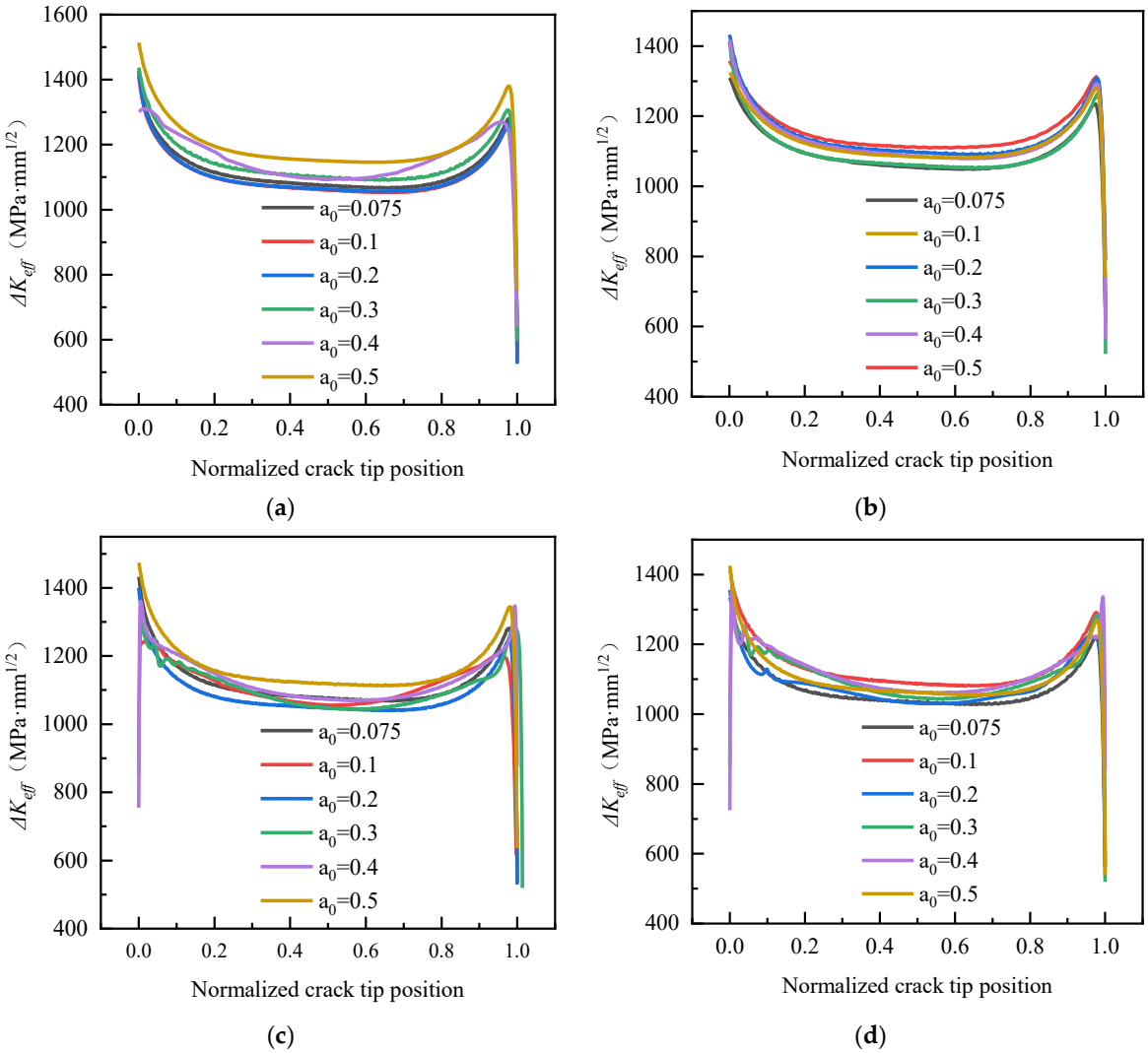


Figure 15. Evolution of stress intensity factors with crack propagation depth. (**a**) R = 0.1, (**b**) R = 0.3, (**c**) R = 0.5, (**d**) R = 0.7.

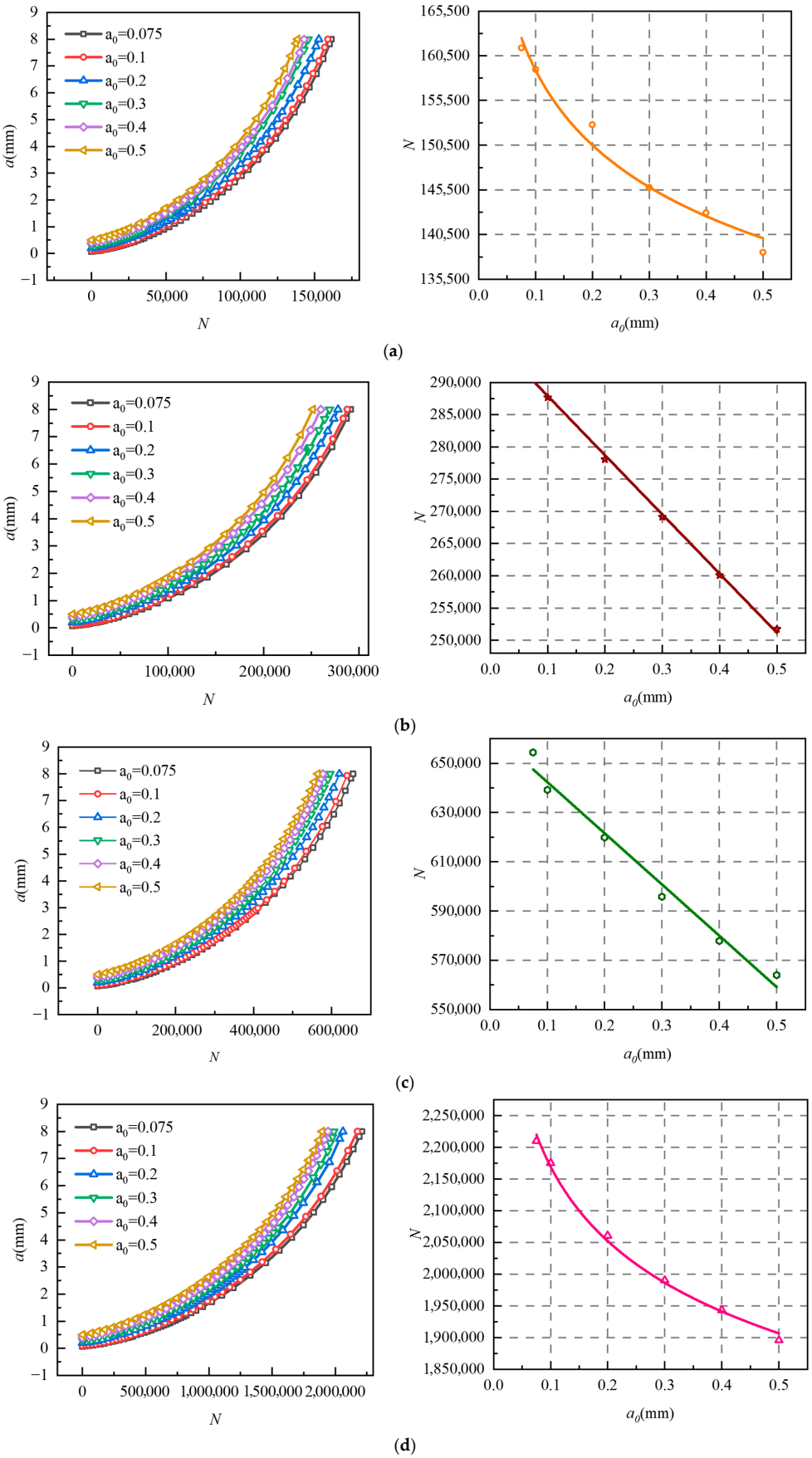


Figure 16. Effect of initial crack size on fatigue life of cruciform fillet weld specimens. (**a**) R = 0.1, (**b**) R = 0.3, (**c**) R = 0.5, (**d**) R = 0.7. The solid colored lines in each sub-figure represent the fitted curves, illustrating the non-linear decreasing trend of fatigue life as the initial crack size (a_0) increases.

Table 4. Maximum ΔK_{eff} values under different initial cracks and stress ratios (MPa·mm$^{1/2}$).

Initial Cracks (mm)	Stress Ratios			
	0.1	**0.3**	**0.5**	**0.7**
0.075	1417	1310	1432	1334
0.1	1410	1358	1242	1412
0.2	1428	1432	1400	1355
0.3	1437	1413	1305	1305
0.4	1310	1418	1361	1366
0.5	1513	1425	1473	1426

Figure 17 shows the normalized fatigue life as a function of initial crack length (a_0) under different stress ratios. Compared with the baseline condition (a_0 = 0.075 mm), a distinct and nearly linear degradation in fatigue performance is observed as the flaw size increases. During the early stage of crack growth (a_0 = 0.1 mm), the effect is limited, with fatigue life remaining between 97.68% and 98.82% of the baseline. In contrast, when the initial crack length (a_0) is 0.5 mm, the fatigue life decreases significantly to 85.78–86.48% of the baseline. Notably, the fatigue life reduction curves for different stress ratios exhibit a high degree of overlap. This insensitivity to stress ratio indicates that the degradation of fatigue life is predominantly governed by the initial defect size, with stress ratio playing only a secondary role in this process.

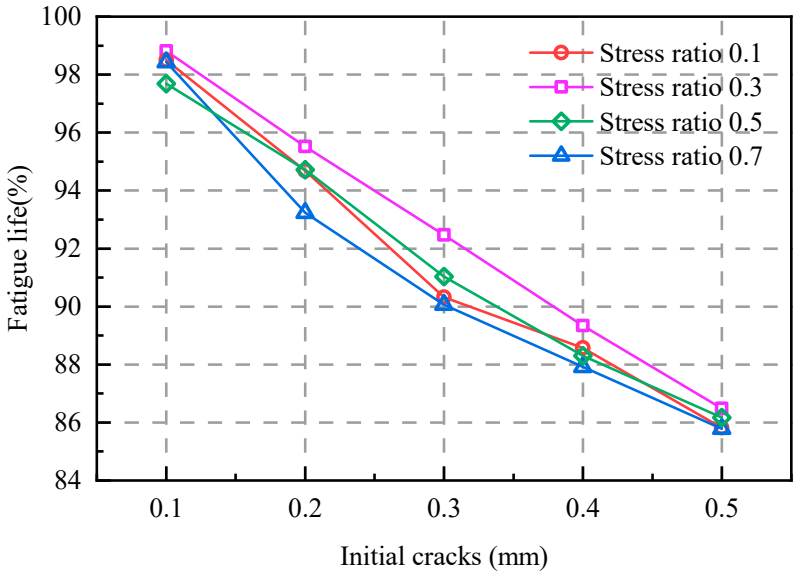


Figure 17. Fatigue life relative to initial crack length 0.075 mm condition.

3.3. Effects of Initial Crack Geometry

With the initial crack depth fixed at a_0 = 0.5 mm, a stress amplitude of 85.5 MPa, and a stress ratio of 0.1, the influence of initial crack geometry was systematically investigated by varying the aspect ratio (a_0/c_0 = 1/5 to 5/5), where c_0 denotes the initial half-length of the surface crack. To reveal the underlying driving mechanisms, the distribution of the effective stress intensity factor range (ΔK_{eff}) along the crack front was first analyzed based on Figure 18. The results show that the ΔK_{eff} distribution curves for different aspect ratios overlap significantly, indicating that the distribution pattern is insensitive to changes in geometry. This insensitivity is further quantified in Table 5, where the maximum ΔK_{eff} values fluctuate only within a narrow range (1379–1415 MPa·mm$^{1/2}$) and do not exhibit a monotonic dependence on crack shape.

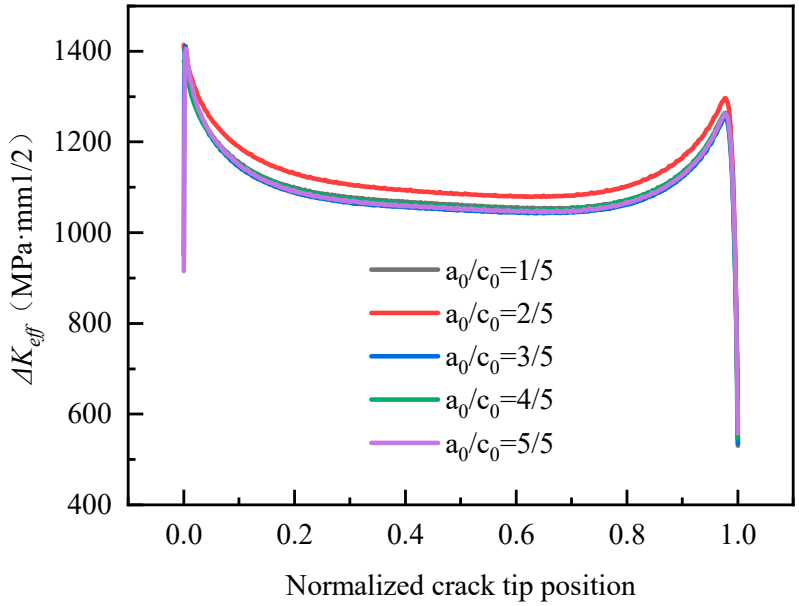


Figure 18. Evolution of stress intensity factors with crack propagation depth.

Table 5. Maximum ΔK_{eff} values under different initial crack geometry.

The maximum crack-tip stress intensity factors MPa·mm$^{1/2}$	**Initial Crack Geometry (a_0/c_0)**				
	1/5	2/5	3/5	4/5	5/5
	1410	1415	1412	1379	1406

Owing to this stable driving force behavior, the resulting fatigue propagation behaviors shown in Figure 19 also exhibit similar trajectories.

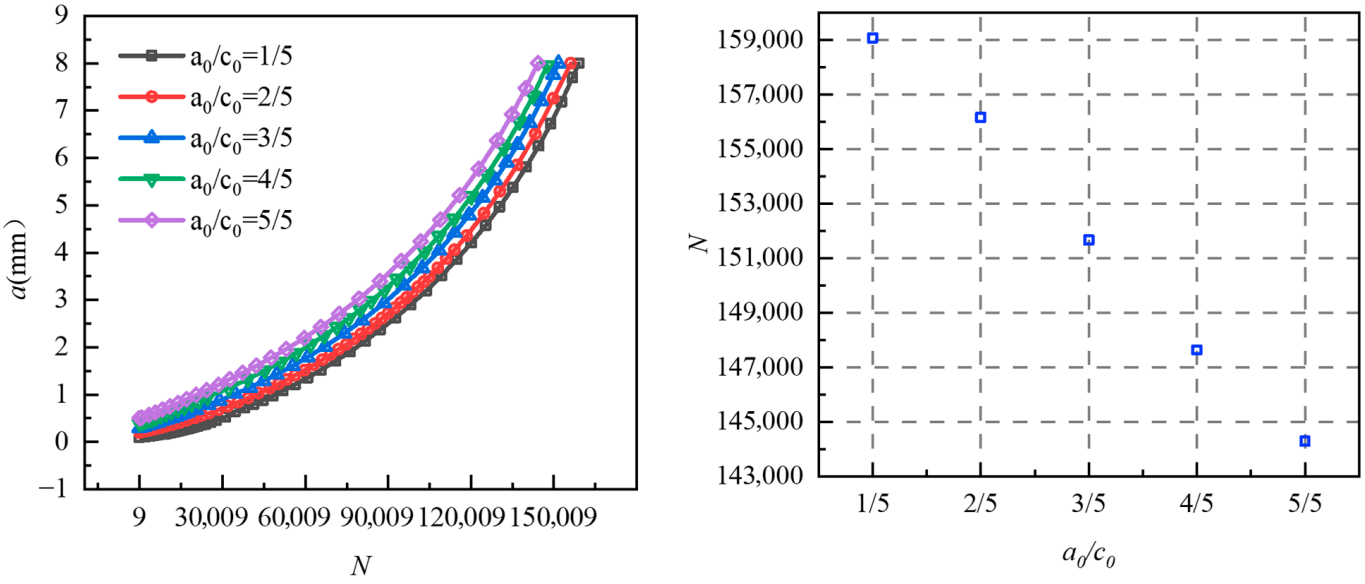


Figure 19. Influence of initial crack geometry on fatigue life of cruciform welded joints. The blue squares represent the calculated fatigue life data points corresponding to specific initial crack aspect ratios (a_0/c_0), illustrating the variation of fatigue life with crack shape.

Figure 20 quantifies the influence of initial crack shape on structural longevity, with the fatigue life normalized against the semicircular baseline crack (a_0/c_0 = 5/5). The results indicate that although flattened cracks (a_0/c_0 = 1/5) provide a fatigue life extension of approximately 10.25%, this advantage decreases significantly to only 2.32% as the

aspect ratio approaches 4/5. Overall, these findings demonstrate that the fatigue performance of cruciform fillet welds exhibits considerable robustness against variations in initial crack geometry.

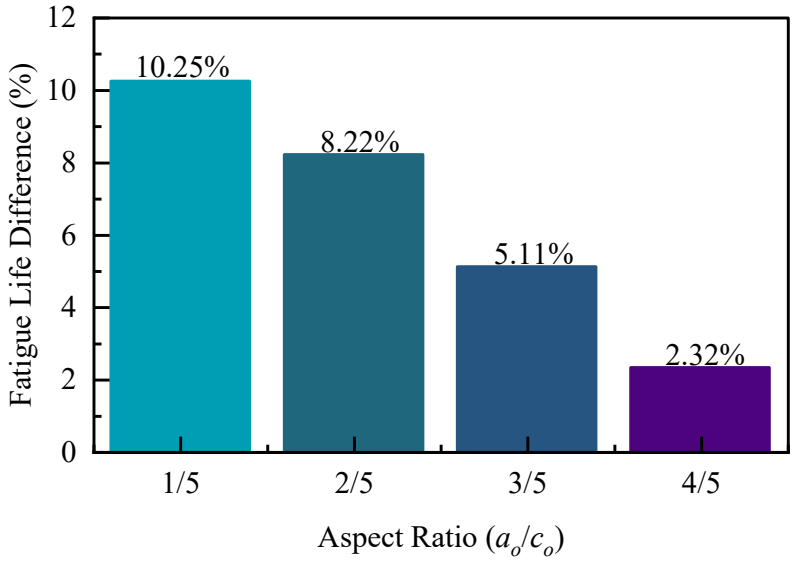


Figure 20. Fatigue life difference relative to aspect ratio 5/5.

3.4. Effects of Initial Crack Location

This section investigates the fatigue behavior corresponding to three distinct initial crack locations: center cracks, boundary (edge) cracks, and cracks positioned at an intermediate "transition" zone. Numerical simulations were performed on semi-elliptical cracks with an initial depth of a_0 = 0.5 mm, under a stress amplitude of 85.5 MPa and a stress ratio of 0.1. Figure 21 shows the distribution of the stress intensity factor range along the crack front, while Figure 22 provides the corresponding *a*-*N* curves and fatigue life comparisons. The maximum crack-tip stress intensity factors for each configuration are summarized in Table 6.

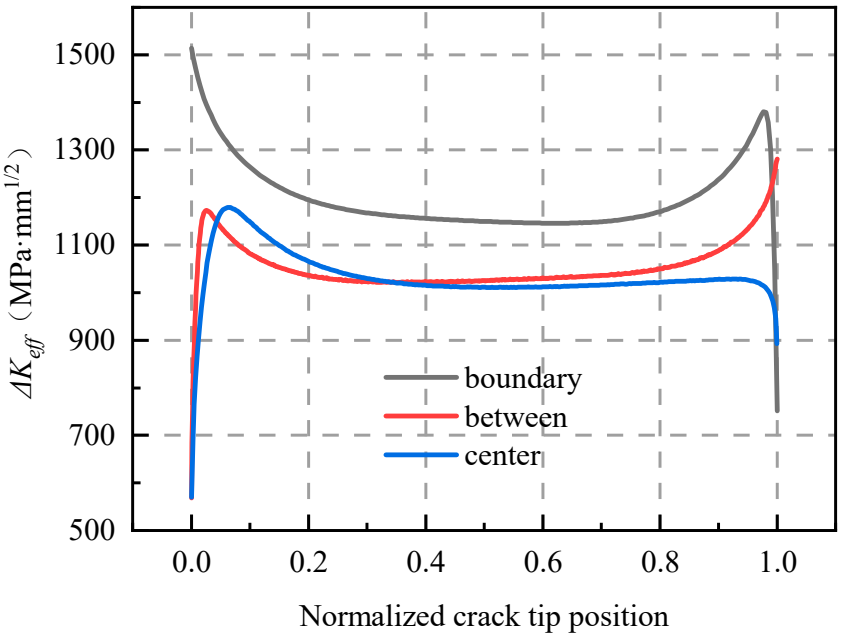


Figure 21. Stress intensity factor evolution with crack depth for different initial locations.

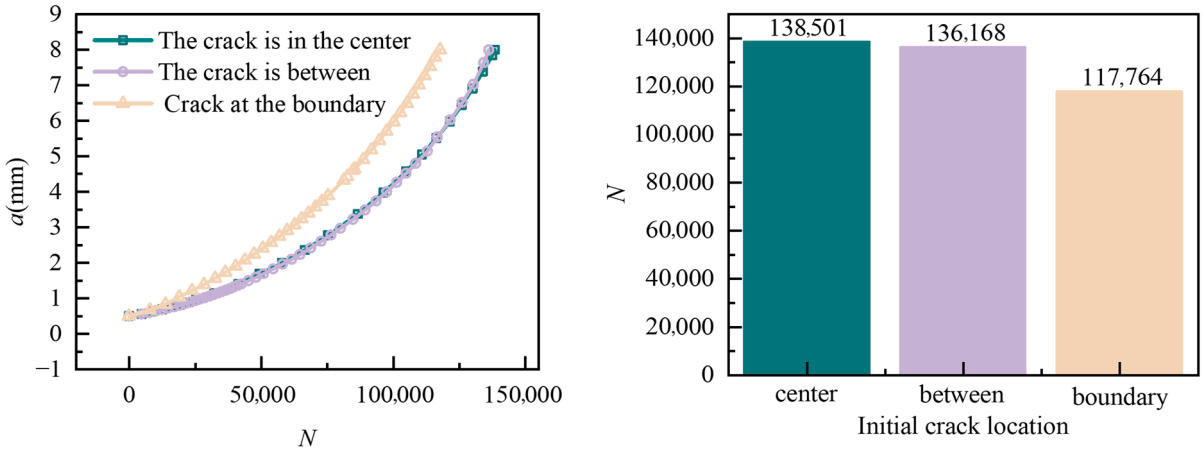


Figure 22. Influence of initial crack location on fatigue life of cruciform welded specimens.

Table 6. Maximum ΔK_{eff} values under different initial crack locations.

The maximum crack tip stress intensity factors MPa·mm$^{1/2}$	**Initial Crack Location**		
	boundary	between	center
	1514	1281	1179

The results indicate that the initial crack location significantly influences the crack driving force. As shown in Table 6, the maximum ΔK_{eff} decreases from 1514 MPa·mm$^{1/2}$ at the boundary to 1179 MPa·mm$^{1/2}$ at the center. This suggests that the geometric stress concentration at the boundary (weld toe) plays a more dominant role in determining the stress intensity factor compared to the constraint effect at the center. Consequently, as the crack location shifts from the boundary toward the center, fatigue life exhibits a clear increasing trend. Mechanistically, this disparity is attributed to the Boundary Correction Factor (γ) in the stress intensity factor formulation. Edge cracks, being situated at the intersection of two free surfaces, experience a loss of surrounding ligament constraint, resulting in a consistently higher γ factor compared to central cracks embedded within the bulk material. In contrast, the influence of initial crack shape (a_0/c_0) tends to diminish due to the phenomenon of "shape convergence," where cracks evolve toward a stable preferred aspect ratio during propagation. Consequently, the persistent boundary effect associated with crack location exerts a more dominant influence on the total fatigue life than the transient effect of initial crack geometry.

As shown in Figure 22, boundary cracks exhibit the shortest fatigue life, whereas center cracks yield the longest. The maximum observed reduction in fatigue life between the center and boundary configurations is approximately 15.2%, decreasing from about 138,500 cycles to about 117,500 cycles. These findings confirm that crack location is a critical parameter influencing fatigue performance. Due to the elevated stress intensity factors associated with free surfaces and geometric discontinuities, boundary cracks are identified as the most critical configuration.

4. Data-Driven Prediction of Stress Intensity Factor Based on Ensemble Learning

4.1. Construction and Feature Engineering of the Dataset

The ABAQUS-FRANC3D coupled approach enables high-fidelity analysis of fatigue crack growth; however, the computational cost associated with adaptive remeshing limits its practical application in fatigue assessment. To bridge the gap between high-precision numerical simulation and rapid engineering prediction, this study leverages the extensive

dataset generated from the parametric analyses in Sections 3.1–3.4 to develop a machine learning-based surrogate model [36–42]. The dataset comprises comprehensive time-series data of crack depth and effective stress intensity factor (ΔK_{eff}) obtained from various simulation scenarios, including different stress amplitudes (67.5–180 MPa), initial crack sizes (a_0 = 0.075, 0.1, 0.2, 0.3, 0.4, 0.5 mm), initial crack shapes (a_0/c_0 = 1/5, 2/5, 3/5, 4/5, 5/5), and initial crack locations (center, edge, and intermediate positions). Since ΔK_{eff} is governed by both loading and geometric constraints, using crack depth (a) alone as input is insufficient. Therefore, a high-dimensional feature vector was constructed, which includes stress range ($\Delta\sigma$), initial crack size (a_0), aspect ratio (a_0/c_0), and a crack location index. Specifically, the location index is quantified using categorical integer encoding, where 0, 1, and 2 correspond to the center, intermediate, and edge cracks, respectively. This feature engineering strategy enables the model to learn the intrinsic mapping between physical boundary conditions and fracture mechanics parameters [43]. Consequently, the final dataset comprises a total of 2000 samples extracted from the valid crack propagation steps across all 15 stress amplitude scenarios.

4.2. Model Construction Based on Ensemble Learning

To accurately capture the highly nonlinear coupling relationships between geometric parameters and fracture mechanics indicators, this study adopts an ensemble learning strategy. Compared to a single machine learning model, ensemble methods enhance overall predictive performance by integrating multiple weak learners. Specifically, four algorithms known for their strong performance in engineering regression problems are employed and compared in this work: Extremely Randomized Trees (Extra Trees), Gradient Boosting, Random Forest, and Bagging with Decision Trees (Bagging (DT)). Among them, the Gradient Boosting Decision Tree (GBDT) based on the Boosting framework and the enhanced variant Extremely Randomized Trees (Extra Trees) based on the Bagging framework demonstrate superior performance in the present prediction model.

4.2.1. Gradient Boosting Decision Tree

GBDT is a typical additive model whose core concept is to iteratively train a series of decision trees to continuously correct prediction errors. The detailed architecture of the GBDT algorithm is illustrated in Figure 23. Unlike traditional models that directly fit target values, each new tree in GBDT aims to fit the pseudo-residuals from the preceding round of the model [44]. The process of the GBDT algorithm adopted in this study is as follows:

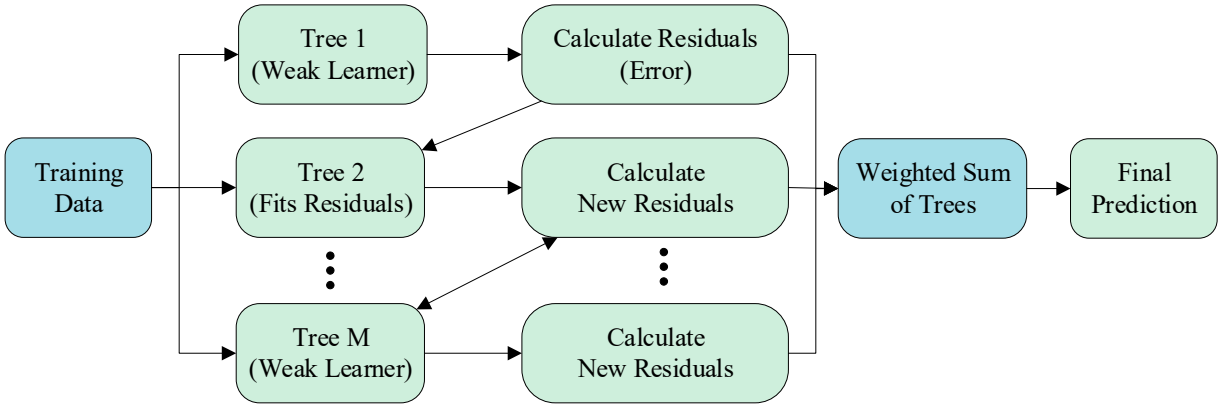


Figure 23. The architecture of Gradient Boosting Decision Tree. The blue nodes represent data states (input or aggregated results), while the green nodes denote processing steps or weak learners. The arrows indicate the logical flow of the algorithm, and the vertical ellipsis signifies the iterative repetition of the boosting process until the M-th tree.

First, initialize the model as a constant $F_0(x)$, which is typically set to the value that minimizes the loss function $L(y,\gamma)$ (such as the mean):

$$F_0(x) = \underset{\gamma}{\operatorname{argmin}} \sum_{i=1}^{n} L(y_i, \gamma) \tag{3}$$

where $F_0(x)$ is the initial model; n is the number of samples; L is the loss function; y_i is the actual target value; and γ represents the constant value intended to initialize the model.

The second step involves iteratively training the model over M cycles. In this study, a total of M = 1200 iterations were performed. In the m-th iteration (m = 1, 2, . . ., M), perform the following:

First, compute pseudo-residuals: calculate the negative gradient direction of the loss function at the current model $F_{\mathrm{m}-1}(x)$, which serves as the pseudo-residual for the current sample i:

$$r_{i\mathrm{m}} = -\left[\frac{\partial L(y_i, F(x_i))}{\partial F(x_i)}\right]_{F(x)=F_{\mathrm{m}-1}(x)} \tag{4}$$

where $r_{i\mathrm{m}}$ denotes the pseudo-residual for the i-th sample at the m-th iteration; $L(,)$ represents the differentiable loss function; y_i is the actual value (ground truth) of the target variable for the i-th sample; x_i denotes the input feature vector for the i-th sample; and $F_{\mathrm{m}-1}(x)$ is the predictive model obtained from the previous iteration (m−1).

Secondly, fit weak learner: use the decision tree $h_{\mathrm{m}}(x)$ of the current iteration to fit the aforementioned pseudo-residuals $r_{i\mathrm{m}}$, capturing the nonlinear mapping relationship between geometric parameters and fracture mechanics indicators.

Then, model update: introduce the learning rate ν to scale the contribution of the weak learner and update the model. In this study, ν is set to 0.05 to prevent overfitting:

$$F_{\mathrm{m}}(x) = F_{\mathrm{m}-1}(x) + \nu \cdot h_{\mathrm{m}}(x) \tag{5}$$

where $F_{\mathrm{m}}(x)$ represents the updated model prediction at the current iteration m; ν is the learning rate used to scale the contribution of each tree; and $h_{\mathrm{m}}(x)$ denotes the weak learner (i.e., the decision tree) fitted to the pseudo-residuals $r_{i\mathrm{m}}$.

After M iterations, the final predictive model $F_{\mathrm{M}}(x)$ is obtained by accumulating the initial model and all weighted weak learners:

$$F_{\mathrm{M}}(x) = F_0(x) + \sum_{\mathrm{m}=1}^{\mathrm{M}} \nu \cdot h_{\mathrm{m}}(x) \tag{6}$$

where $F_{\mathrm{M}}(x)$ is the final strong predictive model after M iterations; $F_0(x)$ is the initial model; and M denotes the total number of iterations in the ensemble.

4.2.2. Extra Trees

To further enhance the model's generalization ability and reduce variance, this study introduces the Extremely Randomized Trees (Extra Trees) regressor. While it belongs to the same Bagging family as Random Forest, Extra Trees incorporates a higher degree of randomness in constructing decision trees. The architecture of the Extra Trees model is presented in Figure 24.

To mathematically formalize the mechanism of the Extremely Randomized Trees (Extra Trees) regressor, let S_n denote the training samples reaching a specific node, and F be the subset of candidate features selected for that node. The algorithm diverges from standard decision trees in its splitting strategy, which proceeds in two steps:

1. Random threshold generation: During the construction of the k-th weak learner $h_k(x)$, unlike conventional methods that search for the optimal cut-point, Extra Trees introduces a stochastic component. For each candidate feature $f \in F$, the split threshold t is not optimized but is drawn completely at random from a uniform distribution within the feature's dynamic range $[f_{\min}, f_{\max}]$ in the sample S_n:

$$t_{\text{random}} \sim \mathcal{U}(f_{\min}, f_{\max}) \tag{7}$$

where t_{random} denotes the randomly generated split threshold for the candidate feature f; $U(,)$ represents the uniform probability distribution; and $f_{\min}$ and $f_{\max}$ correspond to the minimum and maximum values, respectively, of the feature f within the current node sample S_n.

2. Split selection: With the randomly generated thresholds fixed, the algorithm then identifies the best split $\theta^* = (f^*, t^*_{\text{random}})$ by maximizing the impurity reduction score (e.g., Mean Squared Error reduction) ΔI solely among these random candidates:

$$\theta^* = argmax_{f \in F} \Delta I(S_n, f, t_{random}) \tag{8}$$

where θ^* represents the optimal split parameters (specifically the best feature f and the randomly drawn threshold t_{random}); F denotes the subset of randomly selected candidate features; S_n is the set of training samples at the current node; and $\Delta I(\,)$ is the impurity reduction score achieved by the split.

3. Ensemble aggregation: The final prediction $\hat{y}(x)$ is obtained by averaging the outputs of K independently grown trees, utilizing the entire training set to further minimize bias:

$$\hat{y}(x) = \frac{1}{K} \sum_{k=1}^{K} h_k(x) \tag{9}$$

where $\hat{y}(x)$ is the final aggregated prediction for the input vector x; K represents the total number of independent decision trees in the ensemble (in this study, K is set to 1000 or 1200, consistent with your settings); and $h_k(x)$ denotes the prediction output of the k-th individual tree.

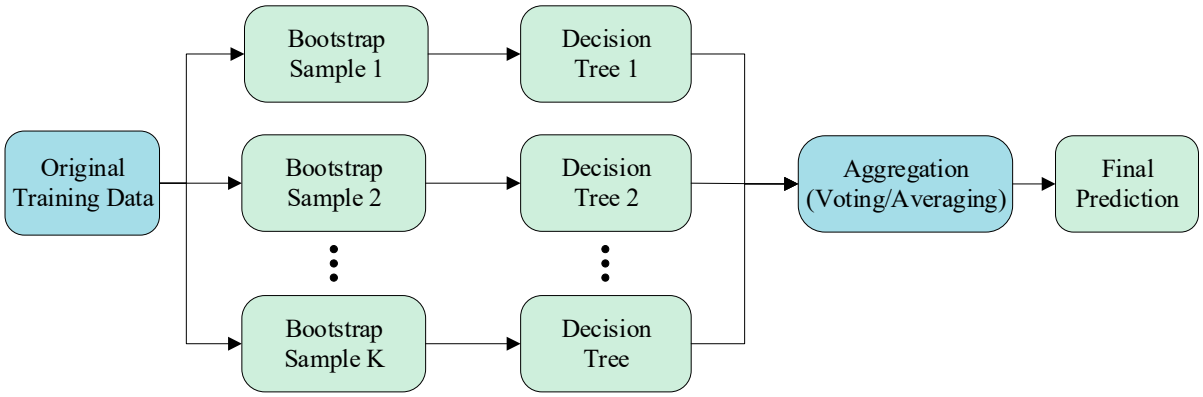


Figure 24. The architecture of Extra Trees. The blue nodes represent the central stages of data input, aggregation, and prediction, while the green nodes denote the parallel ensemble components (bootstrap samples and decision trees). The arrows illustrate the workflow direction, and the vertical ellipsis indicates the parallel generation of K trees.

This mechanism explicitly trades off a slight increase in bias for a significant reduction in variance, ensuring robustness against noise in high-dimensional parameter spaces. Its architecture diagram is shown in Figure 25.

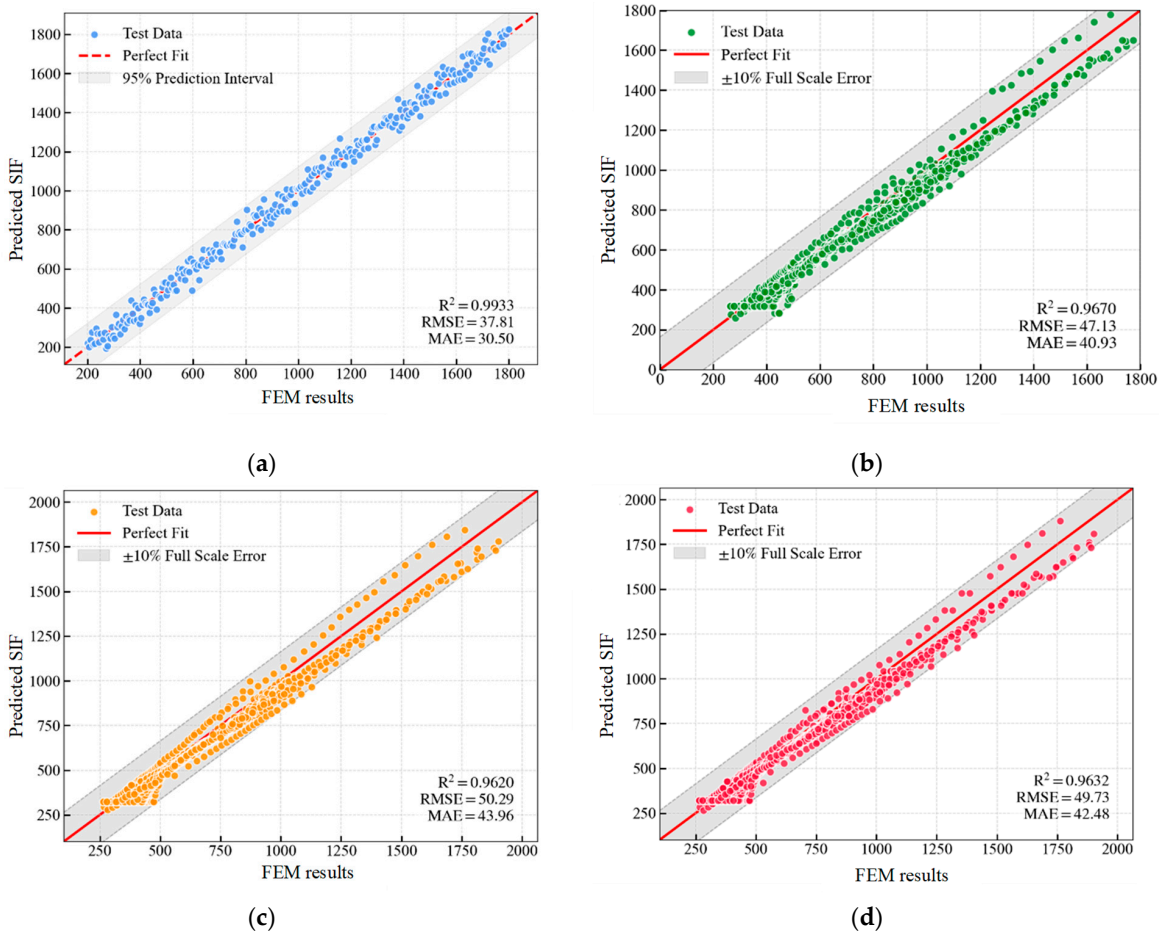


Figure 25. Comparison of predicted vs. FEM-calculated stress intensity factors. (**a**) Extra Trees, (**b**) GBDT, (**c**) Random Forest, (**d**) Decision Tree.

4.2.3. Hyperparameter Optimization

To maximize predictive accuracy, this study employed a rigorous grid search combined with 5-fold cross-validation. The optimization process focused on identifying the optimal balance between model complexity and generalization capability.

The final optimized configurations are summarized in Table 7. The results reveal distinct behavioral patterns among the models: Gradient Boosting (GBDT) required a large number of estimators (1200) combined with a moderate learning rate (0.05) and a constrained tree depth (5). This configuration enables the model to correct errors incrementally in small steps, achieving high precision while avoiding overfitting. Random Forest achieved optimal performance with 800 fully grown trees, effectively reducing variance through large-scale averaging. Bagging (DT) stabilized with 300 estimators using the full sample set. In contrast, Extra Trees converged efficiently with only 100 estimators, demonstrating superior computational efficiency due to its high degree of randomization.

Table 7. Optimized hyperparameters for the four ensemble learning models.

Model	n_Estimators	Max Depth	Learning Rate	Other Parameters	Computation Time (s)
Extra Trees	100	None	-	Min Split: 2	4.25
Gradient Boosting	1200	5	0.05	-	12.60
Random Forest	800	None	-	Min Split: 2	15.82
Bagging (DT)	300	-	-	Max Samples: 1.0	38.30

4.3. Performance Evaluation

To rigorously evaluate the generalization capability of the proposed model, a leave-group-out cross-validation strategy was employed. Specifically, the simulation trajectories corresponding to the stress amplitudes of 94.5 MPa, 99 MPa, and 108 MPa were reserved as the testing set, while the remaining 12 cases formed the training set. This partition resulted in 1802 samples for training and 198 samples for testing, ensuring that the model is tested on unseen loading conditions covering the transition from stable to accelerated crack growth. This partitioning approach ensures that the model predicts fatigue behavior based on learned physical relationships rather than merely memorizing trajectory patterns.

Prediction accuracy was quantified using the coefficient of determination (R^2), root mean square error (RMSE), and mean absolute error (MAE). As shown in Table 8, the Extra Trees model demonstrated superior performance.

Table 8. Performance metrics of machine learning models for SIF prediction.

Model	R^2 Score	Root Mean Square Error (MPa·mm$^{1/2}$)	MAE (MPa·mm$^{1/2}$)
Extra Trees	0.9933	37.81	30.55
Gradient Boosting	0.9670	47.13	40.93
Bagging (DT)	0.9632	49.73	42.48
Random Forest	0.9620	50.29	43.96

The Extra Trees model demonstrated the most robust performance, achieving the highest coefficient of determination (R^2 = 0.9933) along with the lowest root mean square error (RMSE = 37.81) and mean absolute error (MAE = 30.55). These results significantly outperform those of the Gradient Boosting Decision Tree (R^2 = 0.9670) and Decision Tree (R^2 = 0.9632) models, while the Random Forest model exhibited slightly lower accuracy (R^2 = 0.9620). The findings indicate that for the weathering steel cruciform fillet-welded joints studied in this work, the Extra Trees algorithm can explain over 99% of the variance in stress intensity factors, whereas the other ensemble models account for approximately 96%. The superior performance of Extra Trees can be attributed to its unique splitting strategy. Unlike GBDT, which employs a greedy search for optimal cut-points, Extra Trees utilizes random thresholds for node splitting. This mechanism effectively mitigates the risk of overfitting to local irregularities in the simulation data, particularly in the high-SIF regime where gradients are steep. Furthermore, by averaging the predictions of fully grown trees with randomized structures, Extra Trees creates smoother decision boundaries that better align with the continuous physical nature of fatigue crack propagation, thereby achieving higher accuracy and lower variance than the Boosting-based approach. Figure 25 illustrates the correlation between predicted values and actual finite element analysis (FEA)-calculated values. The data points, particularly those corresponding to the Extra Trees model, cluster closely along the 1:1 diagonal. This demonstrates that the proposed data-driven framework can accurately predict instantaneous fracture parameters under complex loading conditions, thereby providing a computationally efficient alternative to repetitive finite element simulations [45,46].

4.4. Model Interpretability and Reliability Analysis

4.4.1. Physical Consistency Verification

Figure 26a,b illustrate the global feature importance for the Extra Trees and Gradient Boosting Decision Tree (GBDT) regressors, respectively. Both models consistently identify crack depth (a) and stress amplitude as the dominant factors influencing the stress intensity factor (SIF). This data-driven finding strongly validates classical fracture mechanics theory,

which describes the proportional dependence of SIF on stress and the square root of crack length ($K = \gamma\sigma\sqrt{\pi a}$) [47]. Notably, secondary parameters—such as initial flaw size (a_0), aspect ratio (a_0/c_0), and crack location—are assigned relatively low importance. This does not imply a lack of physical relevance; rather, it indicates that within the studied parameter space, the variance in SIF driven by geometric shape factors is orders of magnitude smaller than that driven by crack extension and loading. By accurately assigning these secondary weights, the model demonstrates robustness in decoupling complex boundary effects from the primary propagation drivers, effectively filtering out less critical variables and focusing on the governing physical mechanisms.

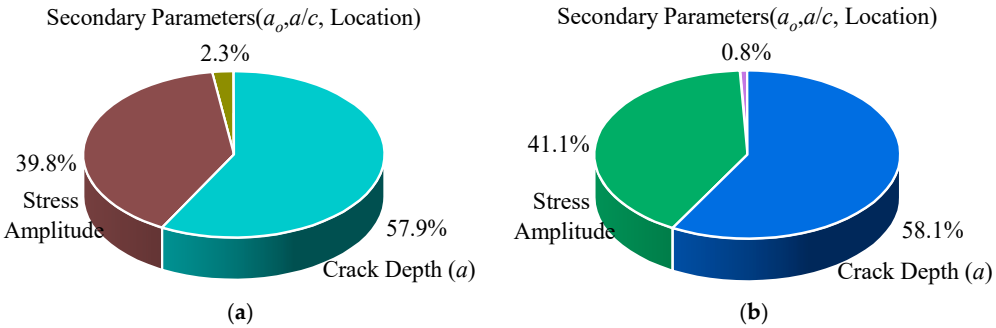


Figure 26. Interpretability analysis: (**a**) Extra Trees, (**b**) GBDT.

4.4.2. Error Distribution and Robustness

To rigorously evaluate prediction accuracy, a residual analysis was performed as shown in Figure 27a,b. The residuals, defined as the deviation between predicted values and finite element analysis (FEA)-calculated benchmarks, exhibit a random scatter without discernible patterns while being balanced around the zero axis. This pattern confirms the model's unbiasedness, indicating that it has successfully captured the underlying mapping without systematic drift across the data range.

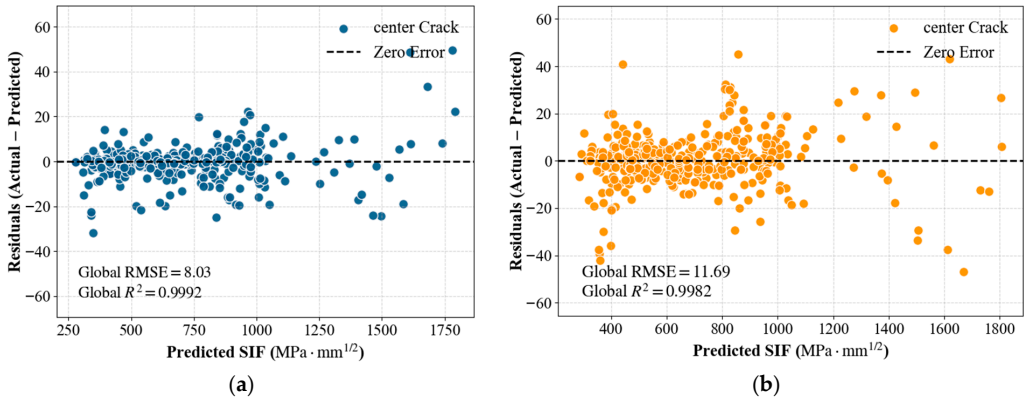


Figure 27. Reliability analysis: (**a**) Extra Trees, (**b**) GBDT.

More importantly, the analysis highlights the model's robustness in high-value regions. As observed in the Extra Trees results (Figure 27a), the residuals exhibit excellent homoscedasticity, maintaining minimal dispersion even in the high-stress intensity factor (SIF) regime. This is particularly significant because this regime typically corresponds to the late stage of fatigue life, where geometric nonlinearities and potential singularities often induce instability in numerical solvers. However, the Extra Trees model maintains a tight error cluster with no distinct outliers. This local stability (RMSE = 8.03 as shown in Figure 27a), alongside the superior overall RMSE of 37.81 MPa·mm$^{1/2}$ (Table 8), strongly

validates the data-driven model's capability to serve as a robust and efficient surrogate for computationally intensive finite element analysis.

4.5. Engineering Application: Fatigue Life Prediction Validation

While accurate prediction of the instantaneous stress intensity factor (SIF) is fundamental, the ultimate goal of engineering assessment is the reliable estimation of a structure's total fatigue life. To validate the practical engineering utility of the proposed Extra Trees surrogate model, this study developed a fatigue life prediction framework by integrating the model-predicted SIF with the numerical integration of the Paris law.

$$N = \int_{a_0}^{a_c} \frac{1}{C(\Delta K)^m} da \tag{10}$$

Figure 28 presents a comparison between the predicted fatigue life based on the machine learning integration method and the benchmark life obtained from high-fidelity finite element (FEA) simulations under various working conditions. The results show a high level of consistency between the data-driven predictions and the physics-based simulation values. As illustrated, all data points converge closely around the 1:1 diagonal line, with the coefficient of determination (R^2) approaching 1000. From an engineering application perspective, it is particularly significant that all prediction points fall entirely within the factor-of-two scatter band, fully meeting the engineering acceptance criteria for fatigue life prediction [48]. This indicates that the cumulative error generated during the recursive integration process is extremely small and practically negligible. These results strongly demonstrate that the proposed framework successfully balances precision and efficiency and is capable of fully replacing costly and repetitive finite element calculations for structural safety assessment. Although the linear elastic fracture mechanics (LEFM) assumption yields conservative estimates under extreme loading (180 MPa), it ensures sufficient safety margins for engineering applications.

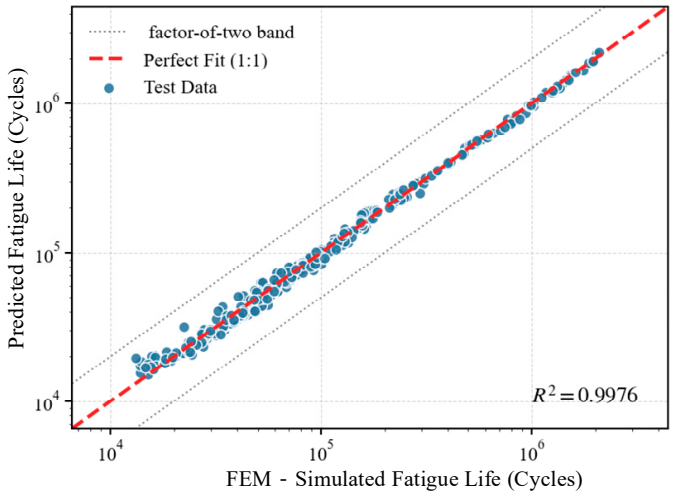


Figure 28. Predicted life vs. FEM-simulated fatigue life comparison chart.

Nevertheless, a balanced assessment of the proposed framework requires addressing both its distinct advantages and inherent limitations. The primary advantage lies in its computational efficiency; the ML surrogate reduces the time cost from hours to milliseconds, enabling real-time fatigue assessment and large-scale probabilistic analyses for digital twin applications. Furthermore, by integrating ML predictions into the physics-based Paris law, the framework maintains physical interpretability, unlike purely data-driven "black-box" models. However, limitations must be acknowledged. First, as a supervised

learning approach, the model's accuracy is strictly bounded by the fidelity of the training data. Second, the current model is specialized for the specific topology of cruciform fillet welds. Application to significantly different structural geometries would necessitate generating new datasets or employing transfer learning strategies, which remains a subject for future research.

5. Conclusions

This study successfully establishes a hybrid framework driven by "high-fidelity numerical simulation + interpretable machine learning" to address the challenges in fatigue assessment of weathering steel welded joints. Through systematic parametric analysis and algorithmic validation, the following main conclusions are drawn:

(1) The simulation framework based on ABAQUS-FRANC3D demonstrates excellent reliability in modeling the three-dimensional crack propagation behavior of cruciform fillet welds. While it is acknowledged that numerical FCG simulations inherently involve uncertainties—primarily stemming from mesh discretization, crack-tip singularity handling, and integration step sizes—the proposed model maintains a validation error of less than 20%. In the context of engineering fatigue analysis, where the standard acceptance criterion is the "factor-of-two" scatter band, this accuracy represents a significant improvement in precision. Crucially, this confirms that the approximation error introduced by machine learning is negligible compared to the intrinsic uncertainties of the fatigue process. Consequently, the model is highly suitable for structural health monitoring, delivering conservative estimates that strictly comply with engineering safety standards.

(2) Although Figure 26 indicates that crack depth has the highest statistical weight in the instantaneous SIF prediction model, the parameter sensitivity analysis reveals that stress amplitude remains the predominant factor controlling the total fatigue life. This is attributed to the power-law relationship in crack propagation theory, where life is highly sensitive to stress variations. When the stress amplitude increases from 67.5 MPa to 99 MPa, the fatigue life is reduced to 40.29% of its original value. Under a stress amplitude of 180 MPa, the fatigue life decreases sharply to 14.28% of the value observed at 67.5 MPa. Within the stress ratio range of 0.1 to 0.7, increasing the initial crack size from 0.075 mm to 0.5 mm reduces the fatigue life by approximately 14% to 15%. The fatigue life for edge cracks is approximately 15.2% shorter than that for center cracks. In comparison, the influence of crack geometry is less significant, with a maximum observed difference in fatigue life of only 10.25%.

(3) Among the constructed prediction models, ensemble learning methods demonstrated superior fitting capabilities for nonlinear fracture parameters. Specifically, the Extra Trees model achieved the best overall performance, with a coefficient of determination as high as 0.9933 and a root mean square error as low as 37.81, significantly outperforming traditional models such as Gradient Boosting Decision Trees. Feature importance analysis further validated the physical interpretability of this model by accurately identifying "crack depth" and "stress amplitude" as the core variables controlling the stress intensity factor. Crucially, these data-driven findings strongly validate classical fracture mechanics theory [46], confirming that the proposed model captures the underlying physical laws of crack propagation rather than merely fitting numerical data.

(4) The proposed "ML-Paris" integrated prediction framework effectively bridges the gap between theoretical simulation and engineering practice. Validation results demonstrate that the fatigue life predictions from this framework align precisely with high-fidelity finite element calculations (R^2 = 0.9976), with all data points falling

within the factor-of-two band. This indicates that the surrogate model, once trained on the generated simulation database, can effectively substitute for time-consuming finite element simulations in rapid assessment scenarios at minimal computational cost, offering an efficient and accurate digital solution for health monitoring and anti-fatigue design of weathering steel bridge structures.

Author Contributions: Conceptualization, J.D. (Jianxing Du) and H.S.; methodology, J.D. (Jianxing Du); software, J.D. (Jianxing Du); validation, J.D. (Jianxing Du), H.S., and J.D. (Jinsheng Du); formal analysis, J.D. (Jianxing Du); investigation, J.D. (Jianxing Du); resources, H.S. and J.D. (Jinsheng Du); data curation, J.D. (Jianxing Du); writing—original draft preparation, J.D. (Jianxing Du); writing—review and editing, H.S. and J.D. (Jinsheng Du); visualization, J.D. (Jianxing Du); supervision, H.S.; project administration, H.S.; funding acquisition, H.S. and J.D. (Jinsheng Du) All authors have read and agreed to the published version of the manuscript.

Funding: This research was funded by the Talent Fund of Beijing Jiaotong University (C23XKRC00010), the Jiangsu Provincial Transportation Engineering Construction Bureau (STE-SJZT-3-05-01), and the National Natural Science Foundation of China (52308132). And the APC was funded by the National Natural Science Foundation of China (52308132).

Data Availability Statement: The data presented in this study are available on request from the corresponding author. The data are not publicly available due to the large size of the finite element simulation files and the proprietary nature of the specific engineering structural details.

Conflicts of Interest: The authors declare no conflicts of interest.

References

1. Su, H.; Wang, J.; Du, J. Fatigue behavior of uncorroded butt welded joints made of bridge weathering steel. *Structures* **2020**, *24*, 377–385. [CrossRef]
2. Lawrence, F.V. Estimation of fatigue-crack propagation life in butt welds. *Weld. J.* **1973**, *52*, 212–220.
3. Azar, A.S.; Svensson, L.-E.; Nyhus, B. Effect of crystal orientation and texture on fatigue crack evolution in high strength steel welds. *Int. J. Fatigue* **2015**, *77*, 95–104. [CrossRef]
4. Hu, L.; Ding, X.; Li, L.; Chen, M.-T.; Zhang, Y. Fatigue behavior of CFRP-strengthened inclined welded steel plates with initial cracks. *Thin-Walled Struct.* **2025**, *209*, 112903. [CrossRef]
5. Hang, T. Research on Stress Intensity Factor Calculation Method of Ship Cruciform Joint Based on XFEM. Master's Thesis, Jiangsu University of Science and Technology, Zhenjiang, China, 2025. (In Chinese)
6. John, S.K.; Cascardi, A.; Verre, S.; Nadir, Y. RC-columns subjected to lateral cyclic force with different FRCM-strengthening schemes: Experimental and numerical investigation. *Bull. Earthq. Eng.* **2025**, *23*, 1561–1590. [CrossRef]
7. Takanashi, M.; Ueda, H.; Saito, T.; Ogawa, T.; Hayashi, K. Development of new design fatigue curves in Japan: Discussion of crack growth behavior in large-scale fatigue tests of carbon and low-alloy steel plates. *J. Press. Vessel. Technol.* **2019**, *19*, 275–283. [CrossRef]
8. Yang, Y.; Meng, Q.; Hu, W. The initial life and short crack propagation life for low carbon steel based on dislocation method. *Adv. Mater. Res.* **2018**, *1145*, 1–7. [CrossRef]
9. Bao, H.; Wu, S.; Wu, Z.; Kang, G.; Peng, X.; Withers, P.J. A machine-learning fatigue life prediction approach of additively manufactured metals. *Eng. Fract. Mech.* **2021**, *242*, 107508. [CrossRef]
10. Zhang, M.; Sun, C.N.; Zhang, X.; Goh, P.C.; Wei, J.; Hardacre, D.; Li, H. High cycle fatigue life prediction of laser additive manufactured stainless steel: A machine learning approach. *Int. J. Fatigue* **2019**, *128*, 105194. [CrossRef]
11. He, L.; Wang, Z.L.; Akebono, H.; Sugeta, A. Machine learning-based predictions of fatigue life and fatigue limit for steels. *J. Mater. Sci. Technol.* **2021**, *90*, 9–19. [CrossRef]
12. Wang, C.Y.; Deng, L.; Zhang, F.; Li, T.; Li, S. Probabilistic machine learning approach to bridge fatigue failure analysis due to vehicular overloading. *Eng. Struct.* **2019**, *193*, 91–99. [CrossRef]
13. Huang, Z.; Chang, D.; Yang, X.; Zuo, H. A deep learning-based approach for crack damage detection using strain field. *Eng. Fract. Mech.* **2023**, *293*, 109703. [CrossRef]
14. Zhang, J.; Zhu, J.; Guo, W.; Guo, W. A machine learning-based approach to predict the fatigue life of three-dimensional cracked specimens. *Int. J. Fatigue* **2022**, *159*, 106808. [CrossRef]

15. Zhang, W.; Su, Y.; Jiang, Y.; Hu, Z.; Bi, J.; He, W. Data-driven fatigue crack propagation and life prediction of tubular T-joint: A fracture mechanics based machine learning surrogate model. *Eng. Fract. Mech.* **2024**, *311*, 110556. [CrossRef]
16. Kamble, R.G.; Raykar, N.R.; Jadhav, D.N. Machine learning approach to predict fatigue crack growth. *Mater. Today Proc.* **2021**, *38*, 2506–2511. [CrossRef]
17. Sun, L.; Huang, X. Prediction of fatigue crack propagation lives based on machine learning and data-driven approach. *J. Ocean Eng. Sci.* **2024**, *9*, 592–604. [CrossRef]
18. Al-Hagri, A.; Katsanos, E.; Stang, H.; Waldbjørn, J.P.; Kolios, A. Fatigue crack propagation and life prediction in offshore steel jackets using multi-fidelity modeling and machine learning. *Eng. Fract. Mech.* **2025**, *332*, 111800. [CrossRef]
19. Huang, X.; Wang, D.; Zhou, J.; Li, M. Application of machine learning in fatigue life prediction of additive manufacturing light alloys. *Chin. J. Nonferrous Met.* **2025**, *35*, 1549–1564. (In Chinese)
20. Xie, C.; Wang, T.; Zhao, S. Fatigue life prediction of turbocharger pipelines based on BO-MLP neural network. *J. Ningbo Univ. (Nat. Sci. Eng. Ed.)* **2025**, *38*, 72–79. (In Chinese)
21. Chen, Z.; Xie, B.; Lu, N. Reliability analysis method of cable bridge structural system based on deep belief network. *J. China Foreign Highw.* **2025**, *45*, 96–102. (In Chinese)
22. Wang, B.; Xie, L.; Song, J.; Zhao, B.; Li, C.; Zhao, Z. Curved fatigue crack growth prediction under variable amplitude loading by artificial neural network. *Int. J. Fatigue* **2021**, *142*, 105886. [CrossRef]
23. Wang, C.; Li, Y.; Tran, N.H.; Wang, D.; Khatir, S.; Wahab, M.A. Artificial neural network combined with damage parameters to predict fretting fatigue crack initiation lifetime. *Tribol. Int.* **2022**, *175*, 107854. [CrossRef]
24. Ma, X.; He, X.; Tu, Z.C. Prediction of fatigue–crack growth with neural network-based increment learning scheme. *Eng. Fract. Mech.* **2021**, *241*, 107402. [CrossRef]
25. Kotousov, A.; Hughes, J.; Khanna, A.; Moreno, B.; Wallbrink, C. Experimental data-driven approach for the evaluation of crack tip opening loads under variable amplitude loading. *Int. J. Fatigue* **2024**, *180*, 108108. [CrossRef]
26. Wang, H.; Fang, X.; Liu, G.; Xie, Y.; Tian, X.; Leng, D.; Mu, W. An approach to predicting fatigue crack growth under mixed mode loading based on improved Gaussian process. *IEEE Access* **2021**, *9*, 48777–48792. [CrossRef]
27. Sharpe, P.S.; Hillberry, B.; Craig, B.A. Fatigue life variability prediction based on crack forming inclusions in a high strength alloy steel. *J. ASTM Int.* **2004**, *1*, 150–163. [CrossRef]
28. Wang, Z.; He, J.; Lu, N.; Liu, Y.; Yin, X.; Xin, H. Experimental and numerical investigation on penetrating cracks growth of rib-to-deck welded connections in orthotropic steel bridge decks. *Structures* **2024**, *61*, 106058. [CrossRef]
29. Pastorcic, D.; Vukelic, G.; Parunov, J.; Bozic, Z. Fatigue life estimation of corroded welded steel joint using probabilistic approach. *Int. J. Fatigue* **2024**, *182*, 108195. [CrossRef]
30. Liu, S.-D.; Zhu, M.-L.; Zhou, H.-B.; Wan, D.; Xuan, F.-Z. Strain visualization of growing short fatigue cracks in the heat-affected zone of a Ni–Cr–Mo–V steel welded joint: Intergranular cracking and crack closure. *Int. J. Press. Vessel. Pip.* **2019**, *178*, 103992. [CrossRef]
31. Haeg, J.; Elfving, F. Potentials and Limitations in Finite Element Based Crack Propagation Analysis Using FRANC3D. Master's Thesis, Chalmers University of Technology, Gothenburg, Sweden, 2020.
32. Bremberg, D.; Dhondt, G. Automatic mixed-mode crack propagation based on a combined hexahedral-tetrahedral approach. *Key Eng. Mater.* **2007**, *348–349*, 581–584. [CrossRef]
33. Su, H. Research on Fatigue Life Assessment Method of Weathering Steel Bridge under Corrosion. Ph.D. Thesis, Beijing Jiaotong University, Beijing, China, 2020. (In Chinese)
34. Liang, R.Z.; Rui, Z.C.; Liang, Z.Y.; Bo, Z.H. M-integral for stress intensity factor base on XFEM. In Proceedings of the Third International Symposium on Electronic Commerce and Security Workshops, Guangzhou, China, 29–31 July 2010; pp. 226–230. Available online: https://ror.org/01xt2dr21 (accessed on 15 January 2026).
35. *BS 7910:2019*; Guide to Methods for Assessing the Acceptability of Flaws in Metallic Structures. The British Standards Institution: London, UK, 2019.
36. Feng, S.Z.; Han, X.; Ma, Z.J.; Królczyk, G.; Li, Z.X. Data-driven algorithm for real-time fatigue life prediction of structures with stochastic parameters. *Comput. Methods Appl. Mech. Eng.* **2020**, *372*, 113373. [CrossRef]
37. Pan, J.; Song, C. Prediction of fracture toughness using small specimens based on machine learning. *Theor. Appl. Fract. Mech.* **2024**, *132*, 104493. [CrossRef]
38. Avilés-Cruz, C.; Aguilar-Sanchez, M.; Vargas-Arista, B.; Garfias-Garcia, E. A new machine learning-based evaluation of ductile fracture. *Eng. Fract. Mech.* **2024**, *302*, 110072. [CrossRef]
39. Zheng, B.; Li, T.; Qi, H.; Gao, L.; Liu, X.; Yuan, L. Physics-informed machine learning model for computational fracture of quasi-brittle materials without labelled data. *Int. J. Mech. Sci.* **2022**, *223*, 107282. [CrossRef]
40. Šodan, M.; Urbanics, A.; Friedman, N.; Stanic, A.; Nikolić, M. Comparison of machine learning and gPC-based proxy solutions for an efficient Bayesian identification of fracture parameters. *Comput. Methods Appl. Mech. Eng.* **2025**, *436*, 117686. [CrossRef]

41. Chaouch, S.; Yvonnet, J. Unsupervised machine learning classification for accelerating FE2 multiscale fracture simulations. *Comput. Methods Appl. Mech. Eng.* **2024**, *432*, 117278. [CrossRef]
42. Feng, Y.; Wang, Q.; Wu, D.; Luo, Z.; Chen, X.; Zhang, T.; Gao, W. Machine learning aided phase field method for fracture mechanics. *Int. J. Eng. Sci.* **2021**, *169*, 103587. [CrossRef]
43. Prokhorenkova, L.; Gusev, G.; Vorobev, A.; Dorogush, A.V.; Gulin, A. CatBoost: Unbiased boosting with categorical features. In Proceedings of the Advances in Neural Information Processing Systems (NIPS), Montréal, QC, Canada, 3–8 December 2018; Volume 31.
44. Friedman, J.H. Greedy function approximation: A gradient boosting machine. *Ann. Stat.* **2001**, *29*, 1189–1232. [CrossRef]
45. Lundberg, S.M.; Lee, S.I. A unified approach to interpreting model predictions. In Proceedings of the Advances in Neural Information Processing Systems (NIPS), Long Beach, CA, USA, 4–9 December 2017; Volume 30.
46. Liao, H.; Sun, X.; Chen, X. A physics-informed residual neural network in the meta-learning framework with non-proportionality measurement for multiaxial fatigue life prediction. *Int. J. Fatigue* **2026**, *203*, 109336. [CrossRef]
47. Lu, J.; Liu, J.; Li, Y.; Hu, J.; Wu, S. Multiaxial fatigue performance of ER8C wheel steel and fatigue life prediction based on MWCM. *Int. J. Fatigue* **2025**, *206*, 109432. [CrossRef]
48. Li, S.; Xie, J.; Zhang, W. A physics-informed data-driven multiaxial fatigue life prediction framework. *J. Build. Eng.* **2026**, *117*, 114859. [CrossRef]

Disclaimer/Publisher's Note: The statements, opinions and data contained in all publications are solely those of the individual author(s) and contributor(s) and not of MDPI and/or the editor(s). MDPI and/or the editor(s) disclaim responsibility for any injury to people or property resulting from any ideas, methods, instructions or products referred to in the content.